Anal Bioanal Chem (2003) 376 : 562–583
DOI 10.1007/s00216-003-1982-2

SPECIAL ISSUE PAPER

Holger Dau · Peter Liebisch · Michael Haumann

X-ray absorption spectroscopy to analyze nuclear geometry and electronic structure of biological metal centers – potential and questions examined with special focus on the tetra-nuclear manganese complex of oxygenic photosynthesis

Received: 3 February 2003 / Revised: 14 April 2003 / Accepted: 15 April 2003 / Published online: 11 June 2003

Abstract X-ray absorption spectroscopy (XAS) has become a prominent tool for the element-specific analysis of transition metals at the catalytic center of metalloenzymes. In the present study the information content of X-ray spectra with respect to the nuclear geometry and, in particular, to the electronic structure of the protein-bound metal ions is explored using the manganese complex of photosystem II (PSIII) as a model system. The EXAFS range carries direct information on the number and distances of ligands as well as on the chemical type of the ligand donor function. For first-sphere ligands and second-sphere metals (in multinuclear complexes), the determination of precise distances is mostly straightforward, whereas the determination of coordination numbers clearly requires more effort. The EXAFS section starts with an exemplifying discussion of a PSII spectrum data set with focus on the coordination number problem. Subsequently, the method of linear dichroism EXAFS spectroscopy is introduced and it is shown how the EXAFS data leads to an atomic resolution model for the tetra-manganese complex of PSII. In the XANES section the following aspects are considered: (1) Alternative approaches are evaluated for determination of the metal-oxidation state by comparison with a series of model compounds. (2) The interpretation of XANES spectra in terms of molecular orbitals (MOs) is approached by comparative multiple-scattering calculations and MO calculations. (3) The underlying reasons for the oxidation-state dependence of the XANES spectra are explored. Furthermore, the potential of modern XANES theory is demonstrated by presenting first simulations of the dichroism in the XANES spectra of the PSII manganese complex.

Keywords Manganese complex · Metalloenzymes · Photosystem · XAFS · XANES

H. Dau (✉) · P. Liebisch · M. Haumann
FB Physik, Freie Universität Berlin,
Arnimallee 14, 14195 Berlin, Germany
e-mail: holger.dau@physik.fu-berlin.de

Introduction

In high-school textbooks it is often stated that in nature only 20 amino acids are needed as building blocks for the proteins which facilitate such an enormous variety of biological functions. This is only half of the truth. Numerous enzymatic functions require that the alphabet of amino acids is supplemented by metal ions more or less tightly bound to the apoprotein. An estimated 30–50% of all enzymes carry protein-bound metal centers located mostly at the center of the catalytic site; essentially all proteins involved in the various bioenergetic pathways (e g., photosynthesis and respiration) are metalloenzymes [1, 2, 3]. Understanding their catalytic function requires detailed insights into the atomic structure of the metal site (arrangement of ligand atoms) and in its electronic structure (oxidation states, orbital occupancies). For characterization of both the atomic and electronic structure of the biological sample, X-ray absorption spectroscopy with synchrotron radiation can be employed [4, 5, 6, 7, 8]. In a recent review, we focused on specific methods to 'watch' biological catalysis at metal sites using BioXAS [7]. Here we will explore the information content of the X-ray absorption spectra with respect to the nuclear geometry and, in particular, to the electronic structure of the protein-bound metal ions.

BioXAS method

At present, BioXAS studies mostly involve measurements at the *K*-edge of protein-bound transition metals [4, 5, 6, 7, 8]. (There are notable exceptions where spectra were collected at the *K*-edge of substrate atoms; for example, XAS at the bromine or selenium *K*-edge to investigate substrate binding [9, 10].) By the choice of a specific *K*-edge, the method facilitates element-specific investigation of the X-ray absorbing atom and its ligand environment. Since investigations on protein samples are exceedingly difficult at low X-ray energies, there are only a few *L*-edge XAS studies on metalloenzymes. If these experimental problems can be mastered, *L*-edge BioXAS studies in the

soft X-ray region can provide insights that are complementary to the information obtainable by *K*-edge XAS [11, 12, 13. 14. 15, 16] since by *L*-edge studies (in contrast to *K*-edge XAS) final states of *s*- and, in particular, *d*-orbital symmetry can also be explored. In principle, BioXAS can be used to investigate protein-bound metal centers of any kind in all states of the enzyme; the method is neither restricted to specific elements nor to specific oxidation states. Metalloenzymes in solution, as well as metal centers in proteins that are embedded in their native membrane environment, can be studied. Today, high-quality BioXAS measurements are also feasible at room temperature using 'quasi-physiological' experimental conditions [17, 18].

Typically, the ratio between the number of investigated metal atoms and host atoms (meaning the atoms of the proteins and the solvent) falls in the range of 10 000–100 000. Mostly due to this extreme "dilution" of the investigated metal ion, BioXAS measurements represent a significant experimental challenge. The involved difficulties can be mastered by using experimental set-ups specifically designed for BioXAS experiments [19]. To cope with the enormous background absorption of the matrix atoms, the excitation spectra of the X-ray fluorescence are mostly recorded using energy-resolving solid-state detectors. Today, using synchrotron radiation, a fluorescence detection mode, and averaging of several energy scans (3–100), high-quality XAS data can be obtained for protein-bound metal centers. At a typical bending-magnet beamline it may take 30–60 min per scan and 12–24 h to obtain a single high-quality EXAFS spectrum. Some modern undulator beamlines (e.g., ID26 at the European Synchrotron Radiation Facility, Grenoble) allow for rapid, synchronous scans of undulator gap and monochromator so that it becomes feasible to collect complete EXAFS scans in time periods as short as 10 s and high quality spectra in 10–20 min (see, e.g., [17, 18, 20]). Seemingly, due to the progress at the synchrotron radiation sources the time period typically needed to obtain one high-quality spectrum is continuously decreasing thereby significantly increasing the potential of BioXAS for time-resolved studies and fruitful investigations on metallonenzymes in various states (semistable intermediates of the catalytic cycle, substrate or pH titrations, etc.; see [7]).

X-ray absorption spectroscopy

In a typical *K*-edge X-ray absorption spectrum of a transition metal complex, the first onset of absorption coincides with transitions of the *1s* core electron to *d*-orbitals. Occurrence of *p*-*d* mixing may result in a dramatic increase of the transition probability of these otherwise dipole-forbidden transitions and, thus, appearance of a resolvable pre-edge peak. The pre-edge peak is followed by the edge region of the spectrum where absorption rises to a maximum, the "edge peak" or "main edge resonance". The structure in the spectra observed within about 40 eV from the onset of absorption, the X-ray absorption near-edge structure (XANES), is determined by transitions to bound states, quasi-bound states, and (partially) localized continuum states with *p*-orbital symmetry. In molecular systems, the XANES states are closely related to unoccupied molecular orbitals (typically of anti-bonding character [21]) as explored in detail in "Results".

The XANES region of the spectrum is followed by the EXAFS range (EXAFS, extended X-ray absorption fine structure) which extends over more than 1000 eV above the onset of the edge-rise. The EXAFS is best understood in terms of short-range scattering theories (for references see [22]). The, in principle, well-established EXAFS analysis [21, 23, 24] represents the primary tool for structural investigations in BioXAS.

The final-state wave function obtainable by scattering theory represents an approximate solution to Schrödinger's equation. This means that, in principle, this approach is not limited to the EXAFS range, but also applicable to the XANES region (for references see [22, 25, 26]). In this case, however, all relevant single and multiple scattering contributions need to be considered. This can be achieved by inclusion of an increasing number of multiple scattering (MS) paths until convergence is reached. This approach has been successfully used (for references see [25]), but convergence is not necessarily reached for a tractable number of scattering paths. Recently, a real-space, matrix-inversion full-multiple scattering (FMS) approach has been presented which avoids the convergence problem of finite-path calculations ([27]; for reviews see [22, 26]). In combination with self-consistent potential calculations, real-space FMS calculation seems to be a particularly promising ab initio method for calculation of XANES spectra. In the "Results" section, XANES calculations using the FMS approach (and code) of Rehr and his coworkers [27] are presented and related to insights obtainable by molecular orbital calculations.

The tetra-manganese complex of photosynthesis

The tetra-manganese complex of oxygenic photosynthesis represents a protein-bound metal complex of outstanding biological importance which has been particularly carefully studied by X-ray spectroscopy [28, 29, 30, 31, 32, 33, 34]. Using this model system (see Fig. 1), we will discuss the information content of EXAFS and XANES in the "Results" section.

Materials and methods

Sample preparation and XAS data collection

PSII-enriched membrane particles and layered XAS samples were prepared as described in [35, 36, 37, 38]. Fluorescence-detected X-ray absorption spectra were collected at beamline D2 of the EMBL Hamburg outstation (HASYLAB, DESY, Hamburg, Germany) at 20 K using a liquid helium cryostat and an energy-resolving 13-element solid-state germanium detector as described in [35, 36].

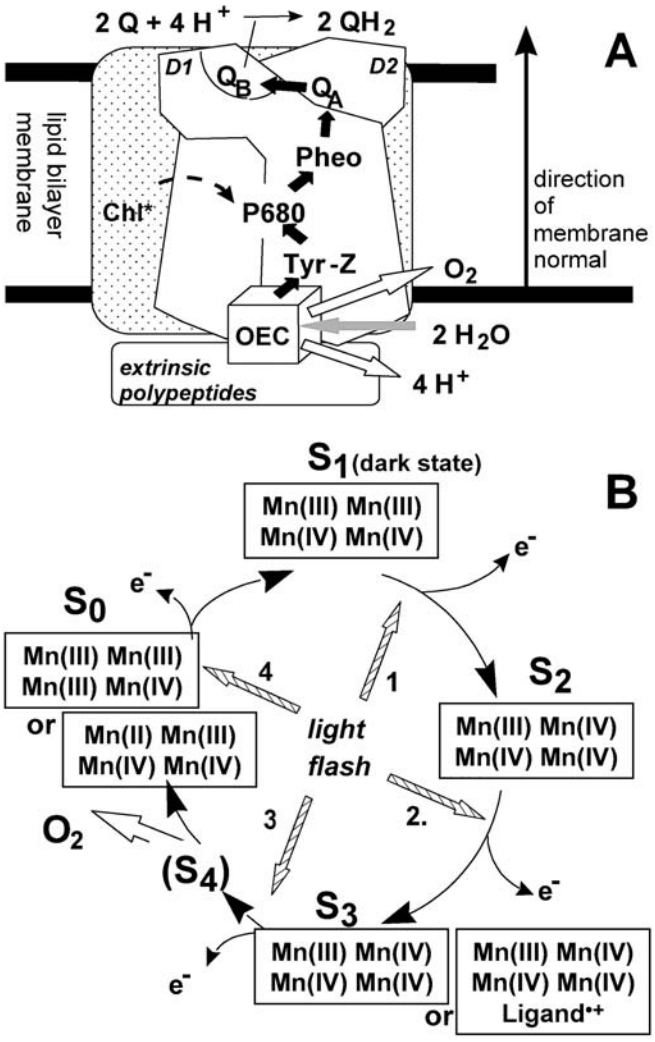

Fig. 1A, B Scheme of the light-induced PS II reactions. **A** Arrangement of the relevant redox factors and electron transport paths, and the direction of the thylakoid membrane normal. **B** S-State cycling of the OEC. Following the absorption of a photon by the PSII pigments and ultra-fast excitation energy transfer to a special set of chlorophylls called P680, electron transfer from P680 to a special pheophytin molecule is initiated. The primary electron donor P680 is re-reduced by a tyrosine residue (Tyr-161 of the D1 protein), and the resulting tyrosine radical delivers one oxidizing equivalent to a part of PSII denoted as oxygen-evolving complex (OEC) or water-oxidizing complex (WOC). Driven by the one-electron oxidation that results from the absorption of a single photon, the OEC advances from the S_n-state to the S_{n+1}-state, where the subscripts give the number of oxidizing equivalents accumulated by the OEC. The most oxidized, semi-stable state of the OEC is S_3; a further one-electron oxidation results in formation of S_4, a hypothetical, transition-state-like intermediate which spontaneously relaxes to the S_0-state concurrently with the release of dioxygen. By application of saturating laser flashes of nanosecond duration (single-turnover flash), the OEC advances synchronously through the cycle by one S-state per flash. For each S-state, possible oxidation states of the four Mn ions are indicated

Integral method for determination of edge positions

The described method has been proposed in [39]. This "integral method" is similar, but not identical, to the calculation of the first moment of the edge spectrum. We define an average edge energy according to

$$E^{edge} = \frac{1}{\mu_2 - \mu_1} \int_{\mu_1}^{\mu_2} E\,(\mu)\; d\mu. \tag{1}$$

In Eq. 1, the inverse function $E(\mu)$ of the spectrum, $\mu(E)$, is integrated. The same value for E^{edge} is obtained by

$$E^{edge} = E\,(\mu_1) + \frac{1}{\mu_2 - \mu_1} \int_{E(\mu_1)}^{E(\mu_2)} \mu_2 - \mu\,(E)\; dE. \tag{2}$$

For experimental spectra, however, $\mu(E)$ is a discrete and, due to noise contributions, possibly non-monotonic function. Consequently, the integration (or summation) limits of the inverse function, $E(\mu_1)$ and $E(\mu_2)$, are not uniquely defined. Therefore, numerical integration is performed using a function $\tilde{\mu}\,(E)$ defined as

$$\tilde{\mu}\,(E) = \begin{cases} \mu_1 & \text{for } \mu(E) < \mu_1 \\ \mu_2 & \text{for } \mu(E) > \mu_2 \\ \mu\,(E) & \text{else} \end{cases} \tag{3}$$

for all energy points within an interval $[E_1,E_2]$:

$$E^{edge} = E_1 + \frac{1}{\mu_2 - \mu_1} \int_{E_1}^{E_2} \mu_2 - \tilde{\mu}\,(E)\; dE. \tag{4}$$

The resulting value of E^{edge} does not depend on the interval borders, E_1 and E_2, if they are chosen in a sensible way (meaning $\mu(E_1)<\mu_1$ and $\mu(E_2)>\mu_2$). However, the E^{edge}-value depends on the parameters μ_1 and μ_2. We have chosen μ_1=0.15 and μ_2=1.00. The first value was chosen to ensure that the magnitude of the pre-edge feature does not affect E^{edge} significantly; the second value was chosen to ensure that the determined edge position is not too strongly affected by the magnitude of the "edge-peak", the more or less broad maximum in $\mu(E)$ following the rising part of the edge.

Advantages of the integral method are:

1. The E^{edge}-value can be determined with high accuracy even for extremely noisy, single-scan data. Thus, this methods allows for an immediate control of X-ray induced photoreduction, an important concern in XAS studies on metalloenzymes.
2. Smoothing of the XANES spectra is not required. If the data is smoothed, E^{edge} is found to be essentially insensitive to the extent of smoothing.
3. The method is relatively insensitive to variations in the shape of the X-ray edge that occur without an overall shift of the edge position.
4. Changes in the determined E^{edge} are in good qualitative agreement with the edge-shift estimated by visual inspection of the spectra (this is mostly not the case for the alternative inflection-point method) and the absolute value typically is close to the energy determined by a simple half-height approach, $\mu(E^{edge})$=0.5.

Multiple-scattering XANES calculations

Simulations were performed using the ab initio full-multiple scattering code FEFF8.2 [27]. For simulation of the $[Mn(H_2O)_6]^{2+}$ spectra, two second-sphere OH groups were considered such that the overall charge of the total cluster was zero. The same potential was used for all atoms of each species. The self-consistent field (SCF) calculations of the potentials in the muffin-tin approximation were performed for a cluster size covering all 23 atoms, while the full multiple scattering (FMS) calculations were done for the first coordination shell only. For the manganese di-μ-oxo dimer, the SCF potential calculations as well as the FMS calculations covered the whole structure consisting of 25 atoms; and the polarization direction was appropriately chosen. Equal potentials were assigned to ligands with equal metal–ligand bond length. Further technical details: muffin-tin overlap of 15%; l_{max}=3; energy-dependent part of the exchange-correlation potential by Hedin–Lundqvist model/ atomic background by von Barth–Hedin model, no imaginary part added; S_0^2 set to unity; correlated Debye model (T_{Debye}=410 K and measurement temperature of 20 K).

Molecular orbital calculations

Molecular orbital (MO) calculations were carried out using the semi-empirical approach of Zerner and coworkers [40, 41, 42] which represents a INDO–SCF method (INDO, intermediate neglect of differential overlap) parameterized to reproduce spectroscopic properties of transition-metal complexes. The restricted Hartree–Fock (RHF) calculations were carried out for a total charge of the complex of +2 and a spin multiplicity of 6 (high-spin state); the σ–σ and π–π overlap weighting factors had been 1.267 and 0.585, respectively. Other spin configurations and configurational interactions (CI) calculations were only used for control purposes, but were not employed for the results shown here. All calculation were carried out on a personal computer using the program Hyperchem (Hypercube, Gainesville, Florida, USA; version 7).

Results and discussion

Extended X-ray absorption fine-structure (EXAFS)

In Fig. 2, the steps are summarized that are typically involved in the extraction of the oscillatory EXAFS [6, 23, 24] from a manganese *K*-edge spectrum collected for the PSII manganese complex in its S_1-state.

Fourier-isolated EXAFS oscillations

The Fourier isolation approach involves the assumption that EXAFS oscillations of a distinct coordination shell can be isolated by back-transformation for a limited range of the *R*-space yielding a $\chi(k)$ function for the chosen co-

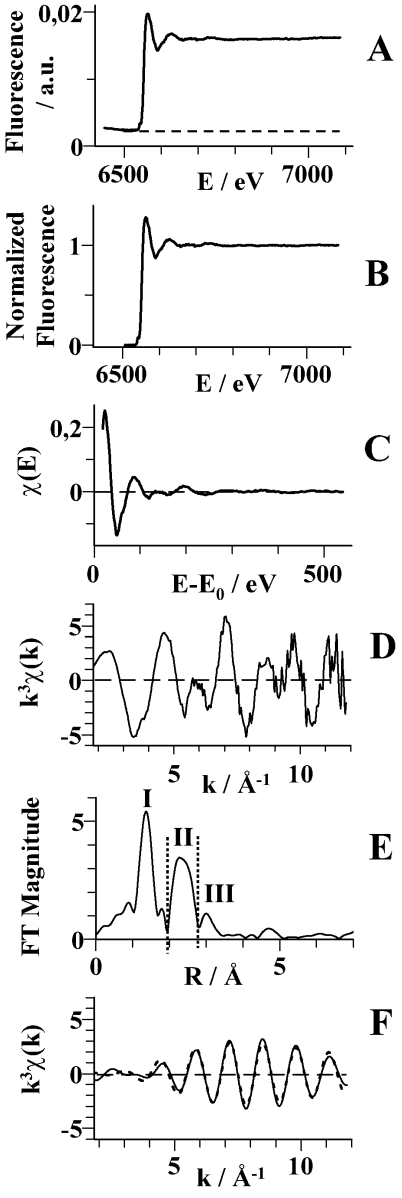

Fig. 2A–F Procedure of extraction of EXAFS oscillations from experimental XAS spectra. **A** "Raw" XAS spectrum of the tetra-Mn complex of PSII in its dark-stable S_1-state. For normalization, firstly the extrapolated pre-edge background is subtracted, yielding $\mu^{Dat}(E)$. Secondly, $\mu^{Dat}(E)$ is divided by a low-order polynomial function which models $\mu_0(E)$, the atomic background absorption yielding the spectrum shown in (**B**). For energies ranging from 20 to 550 eV above the absorption onset, the oscillatory EXAFS structure is extracted by subtraction of either unity or another low-order polynomial function leading to the $\chi(E)$ spectrum (**C**). After selection of an appropriate E_0, the transition from energy to wavenumber scale yields the EXAFS oscillations in the "*k*-space". To compensate for the fall-off (damping) of the EXAFS oscillations with increasing *k*, spectra are often weighted by k^3 to yield $k^3\chi(k)$ (**D**). Fourier transformation (FT) of the $\chi(k)$ yields the FT magnitude as function of the "reduced distance" (*R*) between absorber and backscatterer (**E**); the indicated reduced distance is by about 0.2–0.5 Å shorter than the actual distance between the X-ray absorbing Mn ions and the backscattering atoms. Multiplication of the complex Fourier transform with an appropriate window function (window limits indicated by *dotted lines* in **E**) and backtransformation (inverse FT) yields Fourier-isolated EXAFS oscillation of Peak-II (**F**)

ordination shell. This is exemplified for peak-II of the FT located at R~2.3 Å (Fig. 2E), which is mainly attributable to Mn–Mn distances. The method of Fourier filtering is widely used in the analysis of EXAFS spectra. However, care has to be taken to avoid misleading results. Backscattering shells other then the desired may contribute significantly to the Fourier isolate. If the Fourier isolate shown in Fig. 2F is simulated using a single Mn–Mn distance of ~2.7 Å, its coordination number, $N_{2.7}$, is determined to be 1.6 whereas it refines to ~1.25 in simulations of the whole $\chi(k)$ range, and it is found to be close to unity if more elaborated simulation approaches are used.

EXAFS simulations and the coordination number problem

The extracted EXAFS spectra are simulated according to the "EXAFS equation" [23, 43]. The complex backscattering function and the absorber phase-shift function can be determined by ab initio calculations on the basis of exact curved-wave theory [44, 45, 46, 47, 48]. In addition to the single-scattering EXAFS there may be contributions due to multiple-scattering (MS) paths [46, 49]. Because the "frequency" of the respective EXAFS oscillations (i.e., $2R$ for single-scattering paths) is determined by the total length of the MS path, MS contributions to the Fourier transforms of $\chi(k)$ become prominent only at R greater than ~3.5 Å. In the following, multiple-scattering contributions to the EXAFS are not considered.

Simulation of EXAFS spectra involves the determination of the following parameters by curve-fitting: the (apparent) coordination numbers, N_i (due to the normalization, in multi-nuclear complexes N_i represents the average number of backscatterers "seen" by an X-ray absorbing atom), the distances between absorber and backscatterers, R_i,, and the EXAFS Debye–Waller parameters, σ_i. Frequently, average distances, R_i, between the absorbing atom and the backscattering atoms of the first, second, and occasionally also of higher coordination spheres can be determined with an accuracy of 0.01–0.03 Å [6, 23, 24]. The accuracy in the determined number of backscattering atoms (coordination number), N_i, is often significantly lower (about 25%) because this parameter is highly correlated with the corresponding Debye–Waller parameter (σ_i), which describes the distance spread in the respective coordination sphere. In the case of highly heterogeneous backscattering shells (meaning various types of backscattering atoms or significantly non-Gaussian distance spread within one coordination sphere), it often is difficult to obtain reliable estimates for the coordination numbers N_i without using constraints or additional assumptions (σ_i fixed to physically reasonable values, restriction to chemically reasonable simulation approaches, sequence information, etc.). However, the choice of assumptions and constraints is debatable (as outlined in the following for the Mn complex of PSII).

Figure 3 (left, top trace) shows the Fourier transform (FT) of an experimental EXAFS spectrum of the dark-stable S_1-state of the Mn complex measured at 20 K; the right column shows the respective EXAFS oscillations in the k-space. The FT reveals two mayor peaks at reduced distances of about 1.6 and 2.3 Å which immediately tells us that at least two absorber-backscatterer distances (of about 2.0 and 2.7 Å) can be resolved. As peak-II is relatively large, it is likely due to metal–metal (here Mn–Mn) interactions. A third peak at ~3.2 Å is also well above the noise level. Simulation of this complex spectrum has therefore to involve at least two shells of backscatterers, namely Mn–O,N and Mn–Mn vectors. (In practice, it is almost impossible to distinguish between O and N contributions due to their similar phase functions, whereas sulfur backscatterers can often be distinguished.)

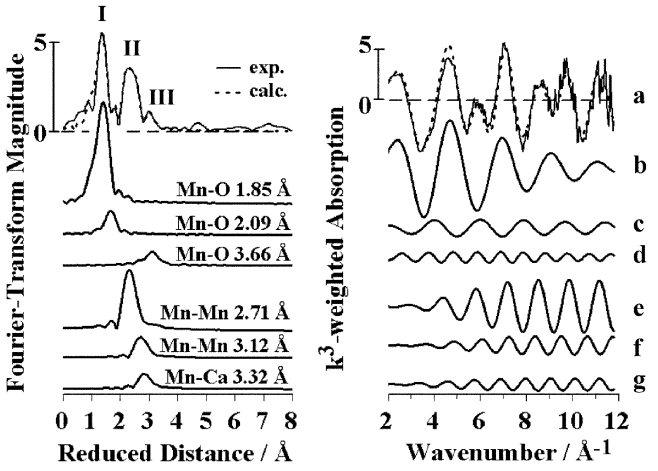

Fig. 3 Simulation of the EXAFS spectrum of the Mn complex. *Left chart*, *upper trace*: Fourier transform (FT) of the experimental spectrum (*solid line*) and result of a six-shell simulation (*broken line*, see Table 1); *lower traces*: the individual FTs of the six simulated backscattering shells. *Right chart*: the respective k^3-weighted EXAFS oscillations in the k-space. Traces a–g are the k-spectra presented in the same order as the respective FTs in the *left chart*

An unrestricted simulation of the experimental k^3-weighted EXAFS oscillations (top trace in the right column of Fig. 3) using only two absorber-backscatterer shells (Mn–O,N and Mn–Mn) yields coordination numbers N_i of 4.10 and 1.29 (Table 1, fit I) and a relatively low fit quality (R_F=25.1%). Both coordination numbers are problematic as discussed in the following section.

First coordination sphere

A value of N_I (O or N backscatterers in the first coordination sphere) of ~4 per Mn atom implies, when taken at face value, a tetrahedral or square-planar coordination of the four Mn atoms in the complex. These coordination geometries are, most likely, incompatible with the XANES spectrum and also highly unlikely from a chemical point of view; a coordination number of 5–6 is clearly more likely.

A more reliable estimate of the coordination number of low-Z scatterers in the first shell of backscatterers may be

Table 1 Parameters obtained by simulations (curve-fitting) of spectra of the Mn complex in its S_1-state. Fits were performed for k^3-weighted EXAFS oscillations (fit range, 20–540 eV above E_0 value of 6547.8 eV; amplitude reduction factor, S_0^2=0.85)

Fit	Shell	N_i (per Mn)	R_i (Å)	$2\sigma^2_i$ (Å^2)	R_F (1–3.5 Å) (%)	Θ_R, angle with membrane normal[d]
I	Mn-O,N	4.10	1.86	0.020	25.1	n.d.
	Mn-Mn	1.29	2.72	0.005		
II[e]	Mn-O,N	5.44	1.86	0.030	18.5	n.d.
	Mn-Mn	0.87	2.71	0.001[f]		
III	Mn-O,N	4.76[c]	1.85	0.019	19.6	n.d.
	Mn-O,N	0.74[c]	2.08	0.008		
	Mn-Mn	1.25	2.72	0.006		
IV[a]	Mn-O,N	3.22[c]	1.83	0.011	19.3	n.d.
	Mn-O,N	2.28[c]	2.00	0.019		
	Mn-Mn	1.29	2.72	0.006		
V	Mn-O,N	4.8[b]	1.85	0.019	9.8	62°
	Mn-O,N	0.7[b]	2.09	0.005		45°
	Mn-O,N	2.5[b]	3.66	0.010		64°
	Mn-Mn	1.06	2.71	0.003		71°
	Mn-Mn	0.5[b]	3.12	0.003[b]		81°
	Mn-Ca	0.5[b]	3.32	0.003[b]		45°

[a]Different value of E_0=6549.4 eV has been used in fit IV
[b]Parameters fixed in the simulation
[c]Coordination numbers coupled to yield a sum of 5.5
[d]Angles of the respective vectors have been determined from the joint simulation of four spectra measured at 15°, 35°, 55°, and 75° (I_{ord}=0.47)
[e]k^1-weighting has been used
[f]$2\sigma^2$ has been restricted to values ≥0

obtained if EXAFS oscillations weighted by k^1 are simulated. Such a fit yields a significantly higher (and more reasonable) value of N_I of ~5.5 (Table 1, fit II). This observation is explainable if we assume that the atoms in the first coordination sphere are not appropriately described by a single backscatterer shell. More than one backscatterer shell seems to be "hidden" in the k^3-weighted EXAFS oscillations such that the partially destructive interference of these oscillations (compare 1.85 Å oscillations and 2.09 Å oscillations in Fig. 3) mimics a low coordination number in simulations of k^3-weighted spectra. Consequently, the next refinement step in the EXAFS analysis is the splitting of the first backscatterer shell into two Mn–O,N shells. Therefore, we fixed the sum of the two first-sphere coordination numbers to the chemically reasonable value of 5.5, also suggested by the k^1-simulations (implying the presence of 5-coordinated and/or 6-coordinated Mn atoms). The use of this approach results in a significantly higher quality of the fit of the k^3-weighted spectra (lower R_F-value, successful simulation of the small satellite peak between peak-I and peak-II).

The two-shell approach to model the first-sphere ligands yields two fit minima with similar R_F-values but clearly different coordination numbers, distances, and Debye–Waller parameters (Table 1, fits III and IV). These apparently different solutions describe a similar distance distribution of the ligands in the first coordination sphere. Not only the average Mn–ligand distance (1.88 and 1.90 Å in fits III and IV, respectively) is similar, but also the overall distance distribution function, which is given by the sum of two Gaussian functions centered at R_i and R_{ii} with widths $\sigma_{ii}$and σ_{ii},, respectively [23] (common peak at 1.85 Å and shoulder at around 2.05 Å, not shown). This means that the two solutions to the fit problem confer essentially the same structural information.

Because several Mn ions in the complex are engaged in di-μ-oxo bridges , Mn–O distances of bridging oxygens and of terminal ligands contribute to the EXAFS. Values for Mn–μO of 1.75–1.85 Å, for Mn(III)–$O_{term.}$ of 1.95–2.30 Å, and for Mn(IV)–$O_{term.}$ of 1.85–2.00 Å can be expected. (Also, it can not be ruled out that a chloride is a manganese ligand [50].) The presence of all these ligands in the first coordination sphere implies a large distance spread. The two fit results (fit III and fit IV) seem to represent alternative descriptions of this distance spread which is, due to its apparent asymmetry, not well described by a single Gaussian function (meaning a single shell of EXAFS backscatters).

At present, a definitive answer towards the question of how to model optimally the EXAFS of the first coordination sphere of Mn in the PSII complex can not be given. Additional information on the direct Mn ligands, possibly from high-resolution protein crystallography data, is needed. In any event, high-quality simulations for chemically reasonable coordination numbers of Mn are only obtainable by using two significantly different distances in the first coordination shell.

Second coordination shell

As discussed elsewhere [7, 34, 38], a Mn–Mn distance of ~2.7 Å is characteristic for di-μ-oxo bridged Mn pairs. Consequently, the value of $N_{2.7}$ gives the number of di-μ-oxo bridges in the Mn complex of PSII, which is of critical relevance for structural models. As shown in Table 1, both the two and the three shell simulations of the k^3-weighted spectrum yield similar Mn–Mn distances of ~2.7 Å and values of $N_{2.7}$ of ~1.25 (fits I, II, IV). It is the latter value (obtained by several groups [32, 33, 34]) that has caused the ongoing discussion on whether $N_{2.7}$ is truly 1.0 [34, 38] or 1.5 [33, 51]. A value of 1.0 suggests that there are two di-μ-oxo bridged pairs in the complex (dimer-of-dimers model) whereas a value of 1.5 could indicate that there are three such pairs.

To obtain clues on the precise value of $N_{2.7}$, we have studied the stepwise disassembly of the Mn complex induced by biochemical treatments [52] or by exposure to a sudden temperature jump [38]. By the latter approach, a series of EXAFS spectra has been obtained which has been simulated additionally taking into account independent information on the presence of longer Mn–Mn distances and of the presence of a Ca atom close to Mn [38, 53, 54, 55]. Thus, a simulation approach could be developed which comprises six shells of backscatterers, namely three shells of O,N atoms, two shells of Mn–Mn interactions, and one Mn–Ca shell [38, 56]. The further coordination shells account mainly for features in the FT that occur above ~3 Å (part of peak-II and the whole peak-III of the FT shown in Fig. 3). These features are not simulated by the two- and three-shell approaches. (From a value of the FT of close to zero at around 3 Å, it can be deduced that interference phenomena due to several EXAFS oscillations with closely spaced frequencies contribute to the spectrum.) Figure 3 depicts the individual contributions of all simulated shells to the EXAFS spectrum. The spectrum is dominated by the Mn–O,N interactions in the first coordination sphere (Fig. 3, trace b) and by the Mn–Mn interactions in the second coordination sphere (Fig.3, trace e). It is clearly seen that the Mn–Mn and Mn–Ca vectors with ~3.1 and 3.3 Å lengths give rise to EXAFS oscillations with similar amplitude and frequency but with a relative phase shift close to 180° (Fig. 3, traces f and g). This means that the contributions of the heavy backscatterers around 3.2 Å to the EXAFS spectrum are extremely small; their presence can be deduced only on the basis of independent information. Table 1 (fit V) lists the simulation parameters that are obtained by the six-shell approach. By the inclusion of three additional shells a significant reduction of the R_F-value (by a factor of about 2 compared to the three-shell approach) to a value smaller than 10% is obtained. It should be noted that the number of free fit parameters is reasonably low only because of the constraints used.

In contrast to the two- and three-shell approaches, the six-shell simulation of the EXAFS spectrum produces a value of $N_{2.7}$ close to one (Table 1), thus indicating the presence of only two di-μ-oxo bridged Mn pairs in the complex. This seemingly clear-cut result, however, might originate from the use of incorrect constraints (with respect to the heavy backscatterers around 3.2 Å). A more unbiased determination of $N_{2.7}$ is certainly desirable. Investigations on the temperature-dependence of the EXAFS spectra did confirm that the EXAFS Debye–Waller factor measured at 20 K is purely of static origin (meaning essentially no dynamic contributions due to vibrational movements at 20 K, unpublished results), but, at least in this particular case, this finding does not contribute to a solution of the coordination number problem.

As noted above, the coordination number (N) and the Debye–Waller factor (σ) are strongly correlated, meaning that different combinations of N_i and σ_i may lead to fits of similar quality. However, the N–σ correlation depends on the k-weighting factor that has been used. It has been shown [24, 57] that for simultaneous simulation of k^1- and k^3-weighted EXAFS oscillations, i.e., minimization of a common error sum, a unique set of N_i and σ_i parameters can be found. To investigate the effect of different k-weighting factors on $N_{2.7}$, the S_1-state spectrum, which has been weighted by either k^1 or by k^3 (Fig. 4A, solid lines), was simulated using an unbiased approach involving only two shells of backscatterers. The value of $N_{2.7}$ was either allowed to vary independently, or was fixed to values between 0.75 and 1.75 (the coordination number of the Mn–O shell was fixed to 5.5). Simulations with unrestricted $N_{2.7}$ yield fit minima at a value of ~1.25 in the case of the k^3-weighted spectrum and of ~0.75 in the case of the k^1-weighted spec-

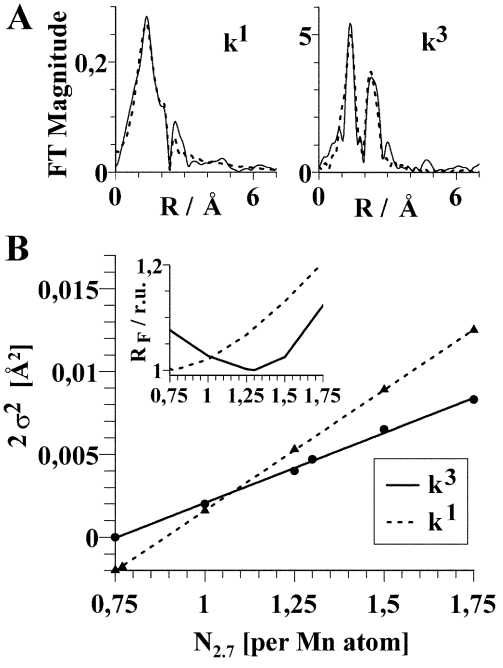

Fig. 4A, B Comparative simulation of k^1- and k^3-weighted EXAFS oscillations of the Mn complex using a two-shell approach. **A** The respective Fourier transforms (*solid line* data, *broken line* simulation). **B** Plot of the Debye–Waller parameters for variation of the coordination number of the Mn–Mn distance of ~2.7 Å ($N_{2.7}$). The *inset* shows the quality factors, R_F, of the respective simulations

trum (Fig. 4A, broken lines). A higher value of $N_{2.7}$ of 0.87 was obtained if the Debye–Waller factor of this shell was restricted to positive values in the k^1 simulation, compare Table 1. Figure 4B shows a plot of the Debye–Waller parameter ($2\sigma^2$) of the 2.7 Å Mn–Mn vector versus $N_{2.7}$. By interpolation of the $2\sigma^2$-values obtained by simulations of k^1- and k^3-weighted spectra, a clear crossing point at $N_{2.7}$=1.06 is obtained. A similar value has been obtained in the six-shell simulation. This value represents the common minimum of the k^1- and k^3-fit. The two error factors (inset in Fig. 4B) also show a crossing point at $N_{2.7}$~1. Using the approach proposed in [24, 57], the simulation of k^1- and k^3-weighted spectra points towards a value of $N_{2.7}$ close to one, implying the presence of two di-μ-oxo bridged Mn pairs in the complex.

In summary, a single experimental EXAFS spectrum carries information on the (average) absorber-backscatterer distances, which are readily determined if well-adapted simulation approaches are used. We estimate that the typical accuracy is better than 0.02 Å for the atoms in the first coordination sphere and for heavy backscatterers in the second coordination sphere. A reasonable accuracy in the determined coordination numbers can be obtained by using elaborated simulation approaches based on independent information from other sources (chemically reasonable motifs, spectroscopic experiments, protein crystallography, etc.). An improvement in the accuracy also can be achieved by the simulation of differently *k*-weighted EXAFS spectra. In the case of the Mn complex of PSII in its S_1-state, such an approach yields coordination numbers of N(Mn–O,N)=5–6 and of $N(\text{Mn–Mn})_{2.7}$=1. Fourier isolation approaches for EXAFS simulation are likely to be misleading when multinuclear metal complexes are considered. Further improvement in the accuracy of the fit parameters may result from the simultaneous simulation of a series of XAS spectra obtained by variation of experimental parameters as outlined in the next section.

X-ray absorption linear dichroism spectroscopy (XALDS)

More reliable structural parameters than obtainable from the analysis of a single EXAFS spectrum can be obtained if several EXAFS spectra are simultaneously simulated under minimization of a common error sum. Such an approach is commonly termed joint-fit or global data analysis (see [38] and references therein). Obviously, these spectra have to be distinctly different. Variations in the EXAFS spectra, which reflect variations in the structure of the metal complex under investigation, may be obtained in time-resolved studies or if sample parameters such as temperature, substrate concentration, assembly state or integrity of the complex, and redox state are continuously varied [7, 38].

Another approach involves the use of non-crystalline, but uni-directionally oriented samples where the metal complex has a preferential orientation in space with respect to the sample normal. Such an orientation can frequently be achieved in the case of membrane proteins. PSII-containing membrane fragments are deposited (by paint-dry techniques [5, 58, 59] or by centrifugation [35, 36] onto a flat surface (typically a polymer foil) in a way that the membrane plane becomes oriented mainly in parallel to the plane of the substrate surface. Using these samples, the linear dichroism can be investigated by collecting spectra at several excitation angles, Θ_E, an approach denoted as angle-dependent XAS, polarized EXAFS, or X-ray absorption linear dichroism spectroscopy (XALDS). In earlier work [60], we have derived a description of the linear dichroism in the EXAFS on the basis of exact curved-wave theory EXAFS [44, 47, 61, 62]. The theory described in [60] allows determination of Θ_R (the angle between absorber-backscatterer value and membrane normal) by a joint-fit of spectra collected for several distinct values of Θ_E (the angle between the electric field vector of the linearly polarized X-ray beam and the sample normal) provided that independent determination of an order parameter characterizing the mosaic spread characteristics has been possible. For perfectly unidirectionally oriented samples $0<I_{ord}<1$; I_{ord}=1. Two advantages are associated with the joint-fit approach: (i) application of the curved-wave theory to EXAFS data obtained for partially oriented systems becomes feasible, and (ii) there is a significant reduction in the number of independent fit parameters (in comparison to separate fits of the individual spectra collected at various excitation angles).

Figure 5 shows the Fourier transforms of two experimental EXAFS spectra of the Mn complex in its S_1-state, which have been measured on partially oriented PSII-membrane fragments at angles Θ_E of 15° and 75°. The two mayor peaks reveal a pronounced dichroism. The finding that the FT magnitudes of both peaks increase at larger angles suggests that the corresponding absorber-backscatterer vectors (R_i) are at angles Θ_R with the sample normal, which are significantly larger than the magic angle (i.e., 54.73° [63]) of linear dichroism spectroscopy. Simulation of four spectra measured at angles of 15°, 35°, 55°,

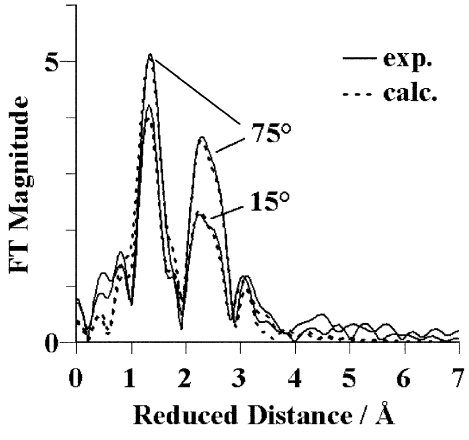

Fig. 5 Fourier transforms of EXAFS spectra of the Mn complex in its S_1-state measured at angles Θ_E of 15° and 75°. The simulated spectra (*broken lines*) have been obtained by using a six-shell approach similar to the one shown in Table 1

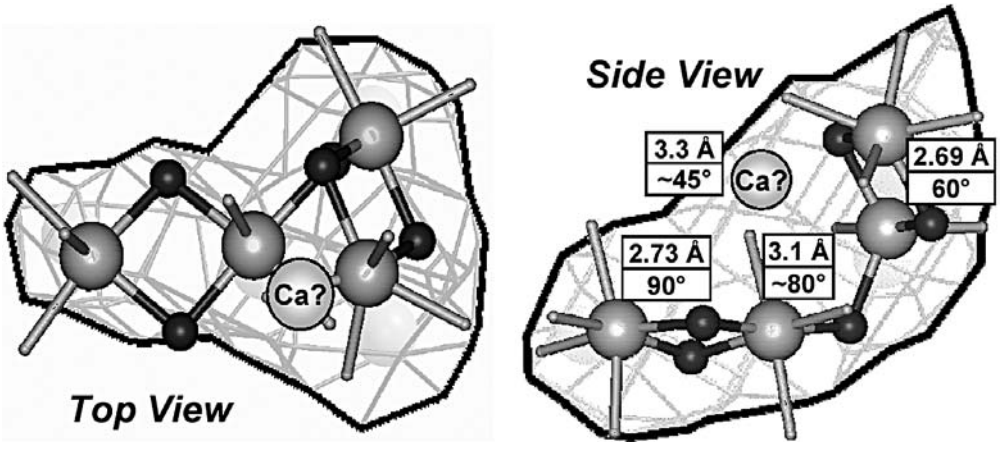

Fig. 6 Structural model of the Mn complex of PSII in the S_1-state. The figure shows the combination of the electron densities derived from protein crystallography (solid surrounding lines and meshes taken from [64]) with the results of EXAFS analysis. *Top view* viewed along the membrane normal onto the membrane plane. *Side view* rotated by 90°. Two di-μ-oxo bridges between Mn atoms and a mono-μ-oxo bridge between the Mn pairs are depicted. The location of the Ca atom is tentative, however, compatible with the EXAFS data [38, 55, 56]. The different lengths of the two Mn–Mn interactions in the di-μ-oxo bridged pairs has been derived from a refined analysis of LD–EXAFS spectra [78] and is in agreement with the results obtained for a partially disassembled complex [38]

and 75° using the above described joint-fit approach and employing six shells of backscatterers (compare Table 1, fit V) yields the Θ_R-values of these distance vectors with the membrane normal (*M*) listed in Table 1. Apparently, the Mn–O,N vectors are at average angles with the membrane normal that are close to the magic angle. All Mn–Mn interactions are roughly perpendicularly oriented with respect to the membrane normal. The putative Mn–Ca vector is at an angle with the membrane normal that is slightly smaller than the magic angle.

Derivation of an atomic resolution model

The construction of three-dimensional models of the atomic structure of the Mn complex has become feasible by combination of the information obtained (i) by analysis of conventional EXAFS spectra, (ii) the angular information from the described dichroism analysis and (iii) by other means (biochemical, spectroscopic, and crystallographic results) [7, 38, 56]. It should be noted that the parameters determined from EXAFS analysis do not allow for the building of a truly unique model. Various steric isomers can not be discriminated nor can the absolute orientation (rotation by 180°) of the complex with respect to the protein matrix be determined from EXAFS data alone. The combination of the recently obtained structural information of the Mn complex from protein crystallography at an intermediate resolution of 3.8 Å [64] with the information from EXAFS analysis [7, 38, 56] suggests a structure of the Mn complex in its S_1-state, as drawn in Fig. 6. Other structural models have been proposed; some of these have been constructed on the basis of different interpretations of XAS data [51, 65, 66]. For a discussion of the dimer-of-dimers arrangement versus the monomer–trimer arrangement see [38]. If the EXAFS coordination number of the 2.7 Å Mn–Mn distance were 1.5, a model involving three di-μ-oxo bridges connecting the four Mn ions would be in agreement with the EXAFS. As discussed above, there is mounting evidence that the EXAFS coordination number is indeed 1.0, suggesting the presence of only two di-μ-oxo bridges, but the above considerations do not represent fully definitive proof. We think that the structural model depicted in Fig. 6 is in good agreement with both protein crystallography and EXAFS data. It represents a useful working hypothesis for the structure of the PSII manganese complex in its S_1-state.

X-ray absorption near-edge structure (XANES)

XANES of Mn oxides and the PSII-Mn complex

In Fig. 7A, the XANES spectra of simple manganese compounds (mostly oxides) are shown. In all these compounds the ligand atoms of the first coordination sphere of manganese are oxygens. The manganese is mostly six-coordinated; only in the permanganate ion do we find four-coordinated manganese in a tetrahedral coordination geometry. The formal Mn oxidation state varies between +2 and +7. Visual inspection of Fig. 7A immediately reveals: (1) An increase in the formal oxidation state is related to a shift of the X-ray edge position to higher energies, and (2) the shape of the spectra in the edge region differs clearly between all the compounds shown. Correlations between the formal manganese oxidation state and edge positions have been confirmed for extended sets of model compounds [28, 32, 67, 68, 69].

XANES analysis has been used for numerous metalloenzymes to obtain insights into the metal-oxidation state and its coordination geometry. In the following we will use the XANES spectra of the water-oxidizing manganese complex of oxygenic photosynthesis as an example that facilitates a detailed discussion of the serious problems involved in the determination of oxidation states by analysis of XANES data.

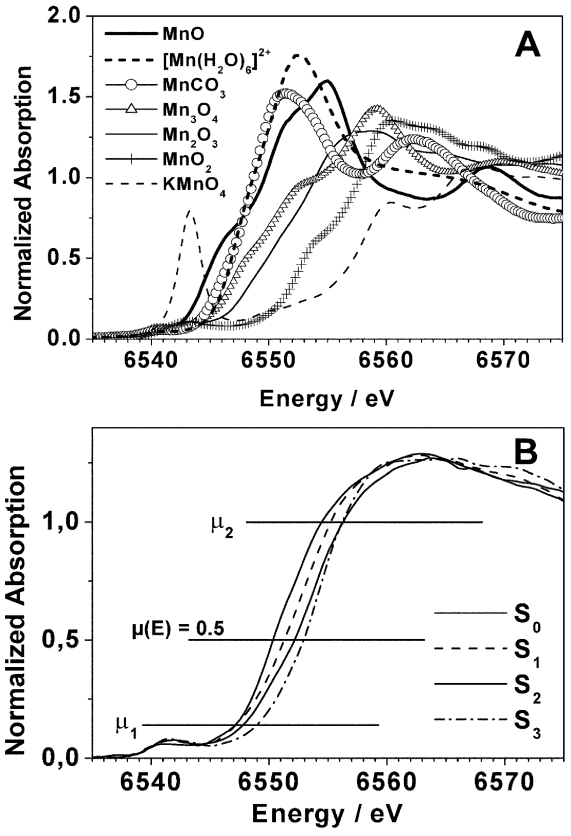

Fig. 7 **A** Mn XANES spectra of seven Mn model compounds (mostly oxides). **B** XANES spectra of the Mn complex of PSII in four S-states. The normalized absorption values, μ_1 and μ_2, represent limits in the integration for the determination of the *K*-edge energy by the integral method (see "Materials and methods")

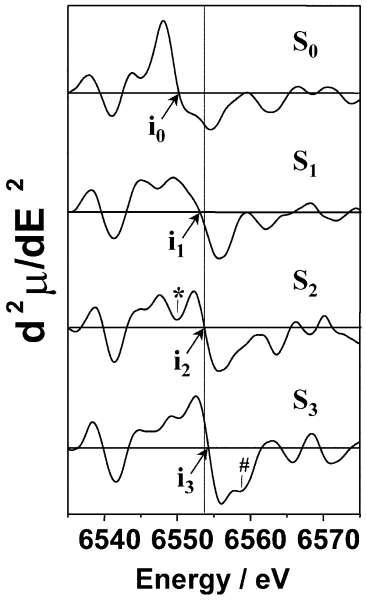

Fig. 8 Second derivatives of the XANES spectra of the Mn complex of PSII shown in Fig. 7B. The inflection-point energies are marked (i_0 to i_3); the *vertical line* is drawn through the first inflection point of the *K*-edge (zero crossing of the 2nd derivative) of the S_2-state spectrum. The *asterisk* marks the position of the shoulder in the S_2-state, which disappears upon the S_2-S_3 transition; the *double cross* labels a shoulder (or peak) appearing in the S_3-state

Figure 7B shows the XANES spectra of the tetranuclear manganese complex of PSII for four different semistable intermediates of the catalytic cycle (for experimental details see Iuzzolino et al. [35]). The spectra shown here correspond to the spectra recently presented in [34]. Visual inspection of Fig. 7B suggests that for each of the oxidizing S-state transitions the absorption edge shifts by 0.5–1 eV to higher energies. An edge-shift of this magnitude can be anticipated for the single-electron oxidation of one out of four manganese ions. However, in addition to the edge-shift, the shape of the absorption edge changes upon each S-state transition (Figs. 7B and 8). In particular, the $S_2 \rightarrow S_3$ transition is accompanied by a significant change in the edge shape. A shoulder present at about 6550 eV in the S_2-state spectrum disappears upon the $S_2 \rightarrow S_3$ transition and a new shoulder (or peak) is formed at about 6559 eV (Figs. 7B and 8). These changes in the edge shape lead to a particularly strong shift to higher energies in the initial rising region of the absorption edge (for $\mu(E)<0.5$, see Fig. 7B) but, in clear contrast to the other S-state transitions, essentially no shift is detected for μ-values around unity.

Determination of changes in the nuclear geometry (structural changes) and electronic structure (metal-oxidation states, orbital occupancies, formation of ligand radicals) is a prerequisite for unambiguous elucidation of the mechanism of photosynthetic water oxidation. In particular, the unresolved question of whether the $S_2 \rightarrow S_3$ transition is linked to a manganese-centered oxidation or whether a ligand radical is formed has led to conflicting mechanistic proposals. In [31, 34, 35] it is concluded that the magnitude of the up-shift of the absorption edge observed upon the $S_2 \rightarrow S_3$ transition is comparable to the edge-shift found for the other oxidizing S-state transitions; consequently manganese-centered oxidation appears to be the more likely option. In [70, 71], X-ray edge positions were defined as the position of the first inflection point (zero-crossing of the second derivative of $\mu(E)$, see Fig. 8) and it was found that the edge-shift observed upon the $S_2 \rightarrow S_3$ transition is significantly smaller than the edge-shift determined for the other oxidizing S-state transitions. This finding has been interpreted as an indication for the absence of manganese oxidation and the occurrence of a ligand-centered oxidation process. Comparison of the recent XANES data by Dau et al. in [34] and by Messinger et al. in [71] shows that there are no major differences in the data itself. Thus, even though similar XANES spectra have been obtained for the S_2- and S_3-state, there are conflicting interpretations with respect to manganese oxidation on the $S_2 \rightarrow S_3$ transitions. The seemingly inconsistent interpretation of similar data highlights the need for a discussion of the information content of the edge spectra. We will present and discuss attempts to relate edge position and shape to the formal manganese oxidation state, the ligand geometry, and the (necessarily closely related) electronic structure.

Empirical approaches to determine oxidation states

To establish an empirical relation between the X-ray edge position on the one hand and the formal oxidation state on the other hand, the edge position is typically quantified, meaning cast into a single energy value. We will discuss three distinctly different approaches to determine this edge energy (E_{edge}):

1. The half-height method, where the value of E_{edge} is equal to the energy corresponding to a μ-value of 0.5 of the normalized spectra (crossing point of the edge spectra and the horizontal line labeled 0.5 in Fig. 7B)
2. The inflection-point method, where the value of E_{edge} is equal to the inflection-point energy, as determined by the (first) zero-crossing point of the second derivative (see Fig. 8)
3. The integral method, where the value of E_{edge} represents the mean value of the energy in the edge region (for details see "Materials and methods")

Figure 9 depicts the correlation between the edge energy and the assumed oxidation state for the edge spectra shown in Figs. 7A and B, using either of the three discussed methods for determination of edge energies. For the set of spectra presented here, a reasonably good, linear correlation between edge energy and (mean) oxidation state is obtained (Fig. 9A, C) by using the integral method or the half-height approach. Edge energies determined by the inflection-point method appear not to correlate well with the oxidation state (Fig. 9B). In the future, we intend to compare the three methods using a more extended set of model compounds.

Since noise contributions to the XANES spectra cannot be fully avoided, extensive smoothing of the spectra is frequently required and the sensitivity of the determined E_{edge}-value to the smoothing procedure needs to be considered. The half-height approach requires interpolation of the discrete spectra to obtain a quasi-continuous function such that the energy value corresponding to a value of 0.5 can be determined precisely. Typically, this interpolation involves moderate smoothing of the spectra. The edge-energy is found to be relatively insensitive to the extent of smoothing (results not shown) unless intermediate peaks or pronounced shoulders are present in the spectra at a μ-value close to 0.5. In such "pathological" cases, however, a pronounced dependence of the E_{edge}-value on the smoothing parameters has to be anticipated. For an appropriate degree of smoothing, the E_{edge}-value is only moderately sensitive to noise contributions.

Using the integral method, smoothing of the experimental results is not required even for highly noisy data sets (see "Materials and methods"). If smoothing procedures are applied, we find the E_{edge}-value to be essentially insensitive to the extent of smoothing (results not shown). Empirically we found that even for low-quality, single-scan spectra the E_{edge}-value can be determined with an accuracy of better than 0.1 eV (see, e.g., [17]; Grabolle et al., manuscript in preparation).

For precise determination of an E_{edge} by the inflection-point method, the second derivative needs to be calculated. Noise contributions are pronouncedly enhanced by calculation of the second derivative, meaning that its calculation without interpolation and significant smoothing is mostly impossible. The edge energies determined by the inflection-point approach are highly sensitive to the extent of smoothing (Fig. 10). As illustrated by the following discussion, this smoothing sensitivity of the inflection-point method is not merely of academic interest, but is one aspect of a long-standing and highly controversial discussion on the character of the $S_2 \rightarrow S_3$ transition of the PSII manganese complex.

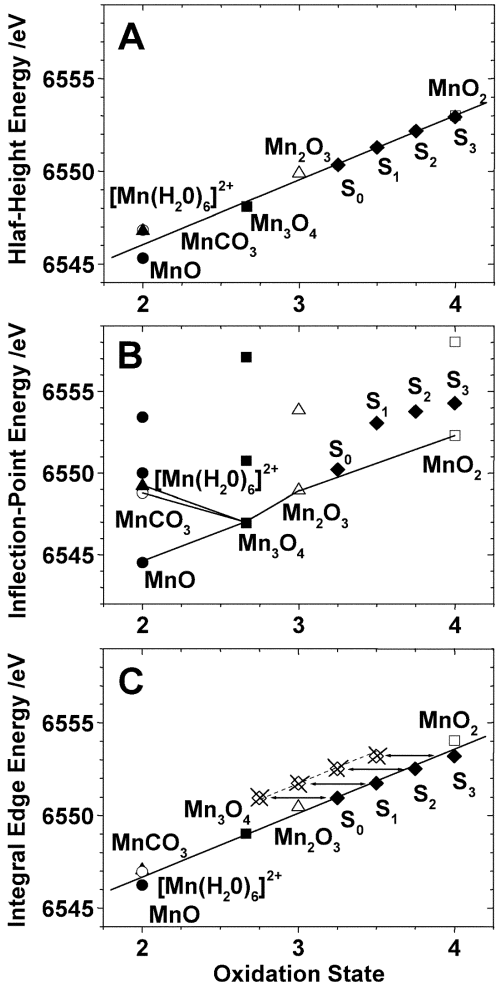

Fig. 9A–C Relation between formal oxidation state and edge energy. The edge energies were determined either by the half-height method (**A**), by the inflection point method (**B**), or by the integral method (**C**). In **B**, for some Mn oxides two or three inflection points were determined; all inflection points are shown, but only the first inflection points are connected by a *solid line*. The presence of the so-called multi-line EPR signal in the S_2-state is suggestive that, in the S_2-state, the average manganese oxidation state is either 3.25, Mn_3(III)Mn(IV), or 3.75, Mn_2(III)Mn_2(IV). The edge energies for the PSII manganese complex are depicted using the second oxidation state assignment for the PSII manganese complex in its S_2-state, i.e., Mn_2(III)Mn_2(IV), and assuming that each oxidizing S-state is coupled to oxidation of one out of four manganese ions. In **C**, both alternatives for the oxidation state assignment of the S_2-state are shown

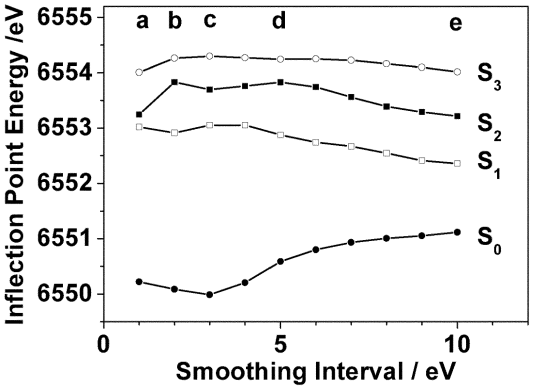

Fig. 10 Inflection-point energies of the XANES spectra of the Mn complex of PSII determined by the second-derivative method (Fig. 8) for various degrees of smoothing prior to derivative calculation

The one-electron oxidation of manganese has been found to be accompanied by an up-shift of the X-ray edge by 2–4 eV ([28, 32, 34, 67, 68, 69, 72]; see also Figs. 7 and 9). Thus, for the oxidation of a single manganese ion in a tetranuclear manganese complex we can anticipate an edge-shift by 0.5 to 1 eV. The $S_1 \rightarrow S_2$ transition is commonly assumed to involve the Mn(III)→Mn(IV) oxidation of a single manganese ion. For this transition we do indeed find an edge-shift around 0.8 eV, which is relatively insensitive to the extent of smoothing. For the $S_0 \rightarrow S_1$ transition, however, the inflection-point approach suggests an edge-shift of more than 1.5 eV for typical smoothing intervals ranging from 1 to 6 eV (see Fig. 10). This means that an unbiased inspection of the inflection-point shift for the $S_0 \rightarrow S_1$ transition is suggestive of a two-electron oxidation, a presumption that is clearly unreasonable in the light of EPR results [66, 73, 74, 75, 76, 77]. For the $S_2 \rightarrow S_3$ transition, it has been reported that the edge-shift is clearly smaller than the $S_1 \rightarrow S_2$ shift [70, 71] whereas others found it to be of comparable magnitude [31, 34, 35]. Using the inflection-point method, depending on the extent of smoothing, both results can be obtained for the same data set. The answer to the question of whether the $S_2 \rightarrow S_3$ edge-shift is significantly smaller than the $S_1 \rightarrow S_2$ shift seems to oscillate between "no" (at *a*, *c*, and *e* in Fig. 10) and "yes" (at *b* and *d* in Fig. 10). In conclusion, the unreasonably large $S_0 \rightarrow S_1$ shift and the extreme smoothing dependence of the $S_2 \rightarrow S_3$ shift indicate that particular caution is advisable when using the inflection-point method for analysis of oxidation-state changes.

The integral method is smoothing-insensitive, but it involves the integration limits μ_1 and μ_2 which had been chosen to be 0.15 and 1.0, respectively ([39, 78]; see also "Materials and methods"). The spirit of the integral method requires that the μ_1-μ_2 interval covers a major fraction of the rising part of the edge, meaning that the difference between μ_1 and μ_2 should be clearly greater than 0.6. Furthermore, μ_1 needs to be positive and $\mu_2(E)$ needs to exist in all relevant sample and reference spectra. Thus, only limited variations of μ_1 and μ_2 are conceivable. To explore the sensitivity of the E_{edge} to the integration limits, the edge positions for the PSII manganese complex in its various S-states were calculated using the most extreme variations of μ_1 and μ_2 that may be still reasonable (Table 2).

Table 2 Influence of the μ_1- and μ_2-parameter of the integral method on the edge-energy values determined for the PSII manganese complex in its various S-states. Edge energies were determined by the integral method for the spectra shown in Fig. 7B using the μ_1- and μ_2-values indicated in the first two columns. The S_1-state edge energy is shown for the dark-stable S_1-state in the third column. The shift in the edge energy obtained for the three oxidizing S-state transitions are given in the fourth to sixth columns

μ_1	μ_2	S_1	$S_0 \rightarrow S_1$	$S_1 \rightarrow S_2$	$S_2 \rightarrow S_3$
0.00	0.85	6549.72	0.60	0.65	0.82
0.00	1.00	6550.45	0.64	0.69	0.71
0.00	1.15	6551.18	0.62	0.75	0.58
0.15	0.85	6551.13	0.78	0.75	0.80
0.15	1.00	6551.74	0.80	0.78	0.68
0.15	1.15	6552.40	0.75	0.83	0.53

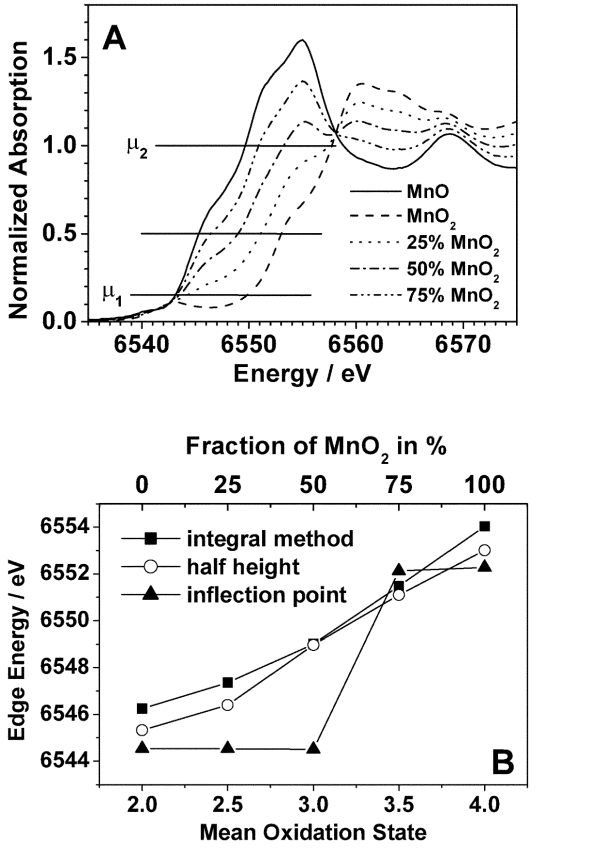

Fig. 11 **A** Experimental XANES spectra of Mn(III)O and $Mn(IV)O_2$ and calculated spectra for three linear combinations of these spectra with different weightings of the compounds (75:25, 50:50, 25:75). The absorption values, μ_1 and μ_2, represent limits in the integration for the determination of the *K*-edge energy by the integral method. **B** The *K*-edge energy as determined by three different methods versus the mean oxidation state of the various Mn(III)O–$Mn(IV)O_2$ mixtures

Inspection of Table 2 reveals that for all combinations of μ_1 and μ_2, the edge-shifts observed upon the $S_0 \rightarrow S_1$, $S_1 \rightarrow S_2$, and $S_2 \rightarrow S_3$ transitions are greater than 0.5 eV and smaller than 0.85 eV, suggesting that sensitivity to the integration limits is reasonably low. Noteworthily, the most pronounced deviation between the magnitude of the $S_1 \rightarrow S_2$ shift and the $S_2 \rightarrow S_3$ shift is obtained for a μ_2-value of 1.15. This μ_2-value is not of general use because the μ-value of 1.15 is not necessarily reached, as demonstrated by the XANES spectrum in Fig. 11 obtained for 50% MnO_2.

The problems in using the inflection-point method for analysis of oxidation-state changes of the PSII manganese complex may be related to the fact that the PSII manganese complex is a tetranuclear complex. The normalized X-ray absorption spectrum of a multinuclear complex containing several X-ray absorbing atoms is obtained by averaging the absorption spectra, $\mu_i(E)$, of the individual X-ray absorbing atoms. In a more general sense, if n species of the X-ray absorbing atom are present, the X-ray absorption spectrum of the sample is given by a linear combination of the individual spectra according to:

$$\mu(E) = \frac{\sum_{i=1}^{n} C_i \mu_i(E)}{\sum_{i=1}^{n} C_i} \tag{5}$$

where $\mu_i(E)$ and C_i denote the absorption spectra and concentrations of the individual species, respectively. For a mixture of species, a method would be useful that relates a parameter, P_{edge}, extracted from the X-ray edges, reasonably well to the averaged oxidation state. This edge parameter should reflect the position of the X-ray edge, but its dimension needs not to be an energy. Ideally, such a method for determination of edge energies is linear in the concentrations of the individual species, such that the P_{edge}-value of the sample equals the averaged P^i_{edge}-values of the individual species. Thus,

$$P_{edge} = \frac{\sum_{i=1}^{n} C_i P^i_{edge}}{\sum_{i=1}^{n} C_i}. \tag{6}$$

The above equation is exactly valid for all methods that involve determination of P_{edge} according to:

$$P_{edge} = \int_{E_1}^{E_2} g(E)\, \mu(E)\, dE. \tag{7}$$

A particularly simple choice would be to use the absorption at a single distinct energy, E_s, in the rising part of the edge as a measure of P_{edge} [meaning $g(E)=\delta(E-E_s)$ and thus $P_{edge}=\mu(E_s)$]. For example, in [18, 20] the absorption at 6551.5 eV is used as a measure of the changes in the mean oxidation state, thus ensuring validity of Eq. 7. However, for an extended set of model compounds the use of $\mu(E_s)$ does not result in good correlation between the P_{edge} and the oxidation state. The definition of a $g(E)$ function that ensures a good correlation between P_{edge} and the mean oxidation is a desirable future development. At present, however, we need to acknowledge that none of the three methods for determination of edge energies obeys Eq. 7, meaning that no method is strictly linear with respect to the species concentrations. Empirically we find that the integral method provides a smooth and relatively linear relation between the edge energy determined for a composite spectrum and the concentration of the individual species, whereas the inflection-point method fails completely in this respect.

In Fig. 11, edge energies were determined for spectra obtained by combining the spectra of Mn(II) in MnO and Mn(IV) in MnO_2. The integral method results in a smooth, slightly curved relation between the mean oxidation state and the edge energy. The half-height method provides a less smooth, but in this particular example, almost linear relation. For the inflection-point method, however, the edge energy stays at exactly the Mn(II) value, up to a Mn(IV)–Mn(II) mixing ratio of 50%; then the edge energy "jumps" to the Mn(IV) value. The complete failure of the inflection-point method in providing an at least approximately linear relation is not explainable by exceptionally pronounced changes in the edge shape. The MnO and the MnO_2 spectra differ clearly in the edge position, but hardly in the edge shape.

Also, for other combinations of spectra we find that the integral method delivers a smooth and approximately linear relation between the mean oxidation state, whereas the inflection-point method mostly fails completely (results not shown). Typically, the half-height method often performs reasonably well, but in some cases pronounced deviations from linearity are observed.

In conclusion, the choice of an appropriate method for determination of edge positions is of clear importance. For multinuclear complexes or other mixtures of several species of the X-ray absorbing atoms, the inflection-point method is clearly not suitable for determination of the mean oxidation state. In contrast, the half-height and, in particular, the integral method seem to provide a relatively smooth and at least approximately linear relation between edge energy and mean oxidation state (but full linearity according to Eq. 6 is achieved by neither method).

To obtain an estimate of the oxidation state of the investigated transition metal system, it may frequently be useful to compare an appropriately determined edge energy with the edge energies of a series of suitable model compounds. However, it remains doubtful whether a general method can be found that relates a single edge energy in a fully unambiguous way to the mean oxidation state of several metal ions in a principally unknown ligand environment. Furthermore, by reducing the highly structured XANES spectra to a single number (e.g., the E_{edge}-value) a vast amount of potentially useful information on the metal site may be lost. We feel that an evaluation of XANES spectra on the basis of an improved understanding of the physical meaning of changes in edge position and shape is desirable. Some aspects of the question of how XANES spectra depend on the ligand geometry and the electronic structure of the metal center are explored in the following section.

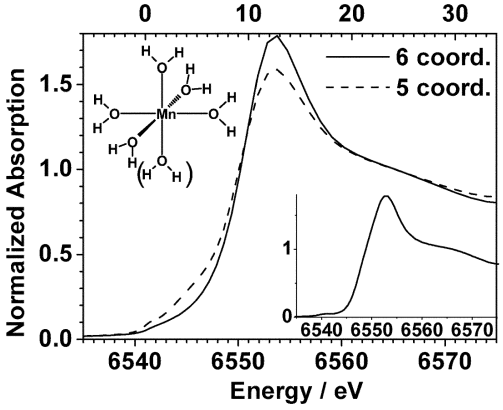

Fig. 12 Calculated XANES spectra for the $[Mn(H_2O)_6]^{2+}$ complex and a hypothetical $[Mn(H_2O)_5]^{2+}$ complex. The five-coordinated complex was obtained by omission of one water ligand of the six-coordinated complex resulting in a hypothetical, perfectly square-pyramidal complex. In both complexes all Mn–O distances are 2.19 Å, a value obtained by EXAFS analysis of an experimental spectrum of the hexaquo complex. The *inset* shows the XANES region of the experimental spectrum of the Mn–hexaquo complex

Simulations approach towards XANES and electronic structure

Using self-consistent potentials and full-multiple scattering calculations as implemented in FEFF8 [27], we calculated XANES spectra for the octahedrally coordinated Mn(II)–hexaquo complex (Fig. 12, for technical details see "Materials and methods"). The ab initio simulations were carried out using standard parameters (see "Materials and methods"); no efforts were made to minimize differences between experimental and calculated spectra by adjusting parameters. As visible in Fig. 12, the calculated spectra resemble the experimental spectrum (inset in Fig. 12) reasonably well.

To investigate the influence of the coordination geometry, one of the six water ligands was omitted without changing the Mn–O distances and bond angles of the remaining five water ligands. Even though the five-coordinated complex does not represent a realistic structure, we did chose this procedure to discriminate between bond-length effects and coordination geometry influences. The following changes are observed upon the transition from the six-coordinated to the (hypothetical) five-coordinated complex:

1. A decrease in the magnitude of the main resonance around 6553 eV (edge peak)
2. Occurrence of a shoulder around 6547 eV
3. An increase in the magnitude of the pre-edge feature at around 6541 eV

The first effect is easily understood in the framework of XAFS-scattering theory; a decreased number of backscattering atoms results in a decrease in the magnitude of the associated scattering resonance. A comparably simple explanation for the second and third effect in terms of scattering theory is not possible.

To obtain insights in the electronic basis of the changes described above and in the relation between the multiple-scattering picture, on the one hand, and the molecular-orbital picture, on the other hand, we carried out MO calculations using the semi-empirical approach of Zerner [40, 41, 42]; for details see "Materials and methods". Again, standard parameters were used and no efforts were made to obtain improved agreements with the experimental results by varying calculation parameters. To relate the virtual MOs to the *K*-edge X-ray absorption the following rationale has been used.

It is assumed that the *K*-edge absorption involves the transition of a single manganese *1 s*-core electron to a partially occupied or fully unoccupied molecular orbital (virtual MO); multiple excitation processes are neglected. Furthermore, it is assumed that the MOs of the Mn ion in its ground state represent a reasonably good approximation to the final-state MOs in the presence of a core-hole. This approximation appears to be relatively severe. However, by MO calculations using the so-called (Z+1)-analogy we find that the influence of the core-hole is not negligible, but sufficiently small to justify its neglect in the context of the present, mostly illustrative calculations. The same holds for the influence of configurational-interaction calculations. In the X-ray spectra, the position of the first maximum (or shoulder) of the weak pre-edge feature (at ~6541 eV) corresponds to the transition to the lowest singly occupied MO, which for high-spin manganese ions is the lowest-lying *3d*-orbital. For comparing energy levels, we use the position of this first pre-edge shoulder as the zero-point of the energy axis of the X-ray spectra and the energy of the lowest-lying singly occupied MO as the energy-zero for the MO energies. The MO energies obtained are shown as labels at the vertical axis of Fig. 13A (six-coordinated Mn) and of Fig. 13B (five-coordinated).

The bar lengths in Fig. 13A and B give the relative contributions of the atomic orbitals (AO) of manganese to the linear combination of AOs used to describe the MOs; selected orbitals are depicted in Fig. 14. For each MO, the sum of the contributions of the manganese AOs and the ligand AOs amounts to unity, meaning that a vanishing bar length indicates purely ligand-centered orbitals. The five lowest-lying MOs are singly occupied whereas all the other MOs in Fig. 14 are unoccupied (virtual) orbitals. The three lowest-lying MOs are almost pure manganese *d*-orbitals of t_{2g}-symmetry; the absence of any ligand contributions (bar length close to unity) indicates that these are non-bonding orbitals. The next two MOs resemble manganese *d*-orbitals of e_g-symmetry; the non-vanishing contribution of ligand orbitals indicates anti-bonding character. In Fig. 14, three groups of degenerate MOs with significant contributions from manganese *p*-orbitals are found (at 9.7, 12.4 and 12.7 eV). These three groups of MOs differ mostly in the orbital coefficients of the water ligands, but they all represent *p*-type anti-bonding orbitals.

In *K*-edge spectra almost exclusively final-state wavefunctions with *p*-orbital symmetry at the X-ray absorbing atom contribute to the transition probability. Therefore,

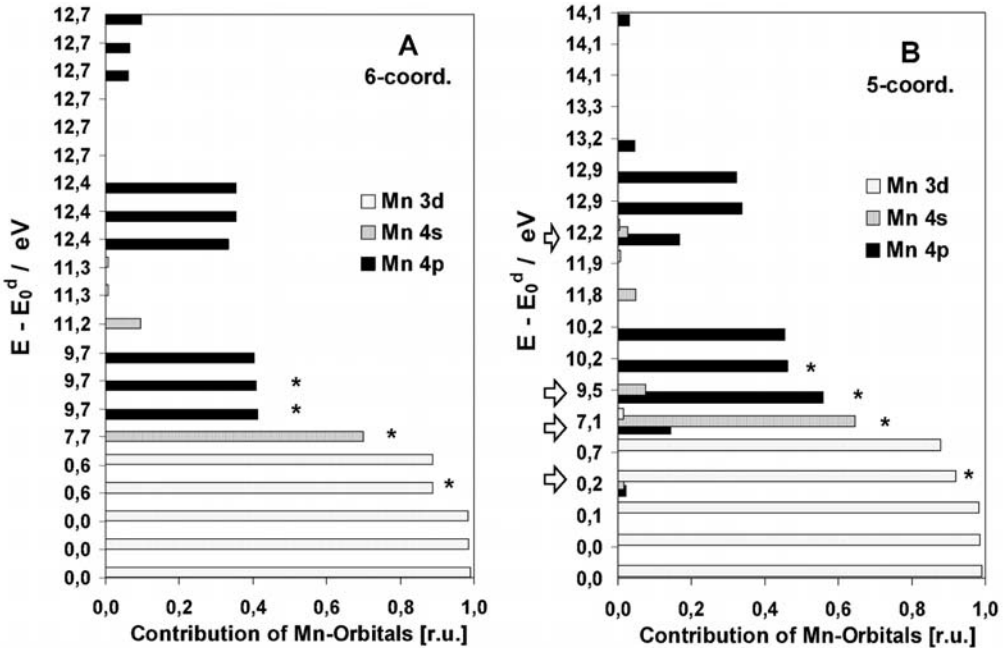

Fig. 13A, B Contributions of AOs of manganese to the singly occupied and fully unoccupied MOs. Calculation were done for: **A** six-coordinated manganese of $[Mn(H_2O)_6]^{2+}$ (octahedral coordination geometry),and **B** five-coordinated manganese of $[Mn(H_2O)_5]^{2+}$ (square-pyramidal coordination). The MOs are linear combination of AOs; the *bar lengths* represent the respective squared coefficients of the AOs of manganese. The squared orbital coefficients are shown for all singly occupied and fully unoccupied MOs; the orbital coefficients of the occupied orbitals are not shown. The MO energies are measured relative to the energy of the lowest-lying, singly occupied MO (E_0^d); these energies are given as labels on the *left side of the bars*. For each MO, the sum of the squared orbital coefficients of manganese and its ligands is unity meaning that shorter bars indicate an increased contributions of the ligand-AOs whereas bar lengths close to unity indicate the absence of significant ligand contributions (non-bonding orbitals). In the five-coordinated complex (**B**), several metal AOs may contribute to a single MO; the four MOs where significant mixing of manganese AOs is observed are marked by an *arrow*. The *asterisks* mark the MOs which are shown in Fig. 14

we assume that, to a first approximation, we will find resonances in the X-ray spectrum at energies which correspond to the MOs with significant contributions of unoccupied manganese *p*-orbitals (black bars in Fig. 13). The contribution of the ligand orbitals to the transition probability is neglected, since the *p*-character of these orbitals with respect to the *1 s* initial-state wavefunction can be assumed to be weak. This means that, according to Fig. 13A, the closely spaced transitions around 11 eV should give rise to a major resonance in the X-ray spectra at around 11 eV (weighted average of the MO energies in Fig. 13), above the first pre-edge shoulder. In the experimental spectra and in the spectra calculated by means of multiple-scattering (MS) theory the dominating resonance (edge peak) is found around 12 and 13 eV, respectively.

The above rationale involves relatively severe approximations; the surprisingly good agreement between the MO calculations and the experimental results might be partially fortuitous. Nonetheless, the MO calculations illustrate that the main X-ray resonance can be assigned to transitions to anti-bonding MOs with significant contributions of atomic *4p*-orbitals of the X-ray absorbing manganese. Because no π-character of these antibonding MOs is detectable (see Fig. 14), the main edge resonance can be considered to be a σ*-resonance (at least in this particular example).

The transition to the five-coordinated complex changes the orbital occupancies significantly (Fig. 13B). Whereas essentially no mixing between manganese orbitals is observed for the six-coordinated complex, we obtain significant *s-p* and also some *p-d* mixing in the five-coordinated complex. In particular, the anti-bonding *s*-orbital at ~7 eV gains significant *p*-character and a small amount of *s-p-d* mixing is observed for one of the anti-bonding *d*-orbitals. Thus, the MO calculations predict a resonance in the X-ray spectrum at about 7 eV and a small increase of the pre-edge magnitude. These predictions seem to be in agreement with the results obtained by scattering theory (Fig. 12). The *s-p* mixing of the MO at ~7 eV can explain the shoulder in the rising part of the X-ray edge (at 5–8 eV), which had been calculated for the five-coordinated complex by scattering theory. Therefore, we assign the shoulder in the multiple scattering calculations of the five-coordinated complex to pronounced *s-p* mixing of manganese *4p*-orbitals, a necessary consequence of the transition from the symmetrically six-coordinated complex to the five-coordinated complex with square-pyramidal coordination. The small increase of the pre-edge peak predicted by the MS calculations for the five-coordinated complex (see Fig. 12) seems to correspond to the increased *p-d* mixing found by the MO calculations.

The above considerations demonstrate that, with respect to the position of resonances, the MO calculations result in predictions that are consistent with the results of advanced ab initio calculations done in the framework of MS theory. Both methods represent approximate solutions

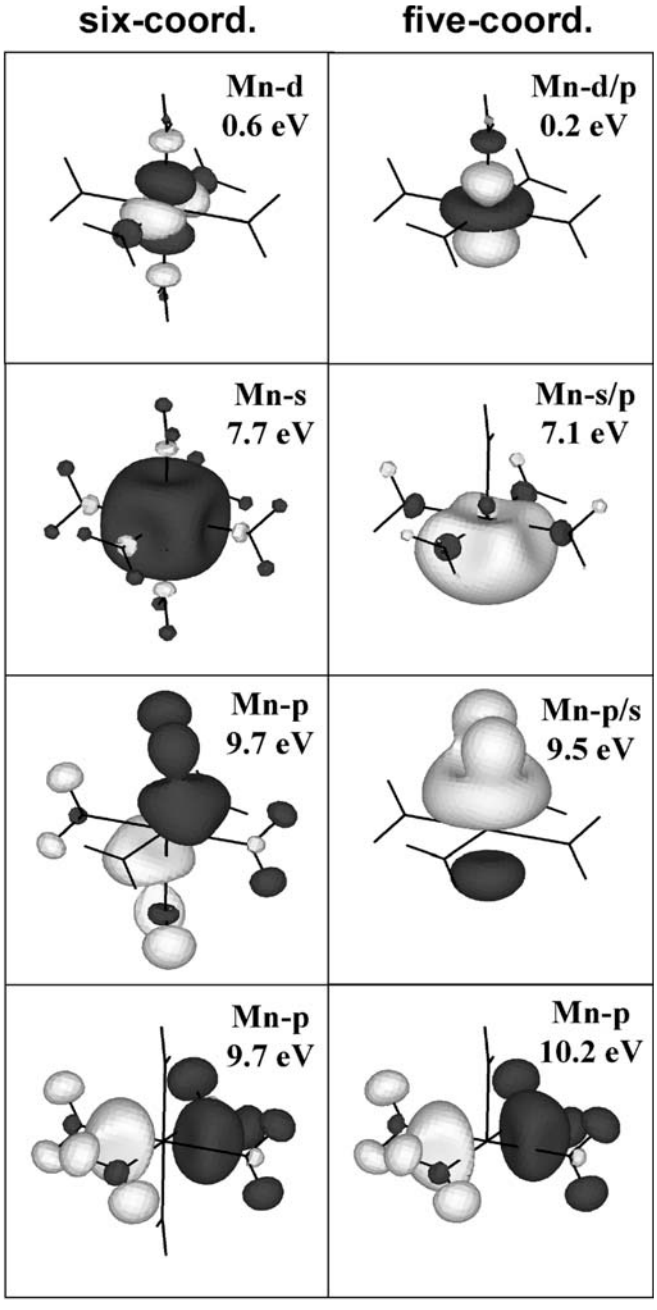

Fig. 14 Selected MOs of the six-coordinated (*left row*) and the five-coordinated (*right row*) manganese complex. In the contour plots (contour level of 0.045), the contour surface is either light or dark shaded to indicate the sign of the wave-function in the respective region. For further details, see legend of Fig. 13

of Schrödinger's equation for a complex multi-electron problem. The scattering theory focuses on the description of the semi-bound and continuum states of the photoelectron, whereas the chemical bonding is only considered in a highly approximate way. The MO approach focuses on the MOs of localized bonding and anti-bonding states. In contrast to scattering theory, the MO approach does not readily provide a full XANES spectrum. To obtain a XANES spectrum, a (more or less empirical) convolution of the resonances of the MO calculations is required to simulate the superposition and mixing of the MO-predicted localized states and the continuum states [79, 80, 81]. Therefore, in general, scattering theory seems to be the more natural approach to obtain a description of the XANES spectra. We feel that its combination with MO calculations may turn out to be useful to translate features observed in the XANES spectra into information on the MO structure of the metal center.

The analysis of changes in the XANES spectra may facilitate conclusions on changes in the coordination geometry. For example, the changes in the XANES spectra predicted for a transition from five- to six-coordinated manganese resemble qualitatively the changes observed upon the $S_2 \rightarrow S_3$ transition for the PSII manganese complex (Fig. 7B), thus supporting the hypothesis presented elsewhere [34].

In the following section, the influence of bond lengths and oxidation state changes is investigated using the multiple scattering approach.

Simulations on the bond-length/ oxidation-state dependence

In the six-coordinated complex discussed above, the Mn–O bond length was varied and spectra were calculated (Fig. 15A). We observe a pronounced bond-length dependence of the resonance position and, consequently of the X-ray edge (Fig. 15B). Experimentally [82, 83, 84] and theoretically [81, 85] a bond-length dependence of the resonance position has been derived for various elements. Mostly the relation between the resonance position, E_{res}, and the bond length, R, has been found to follow the equation:

$$E_{res} = A + B/R^2. \tag{8}$$

The lines in Fig. 15B were obtained by using Eq. 8. Using simplified scattering considerations, the bond-length dependence of the XANES spectra can be easily understood if we consider, to a first approximation, the peak-resonance to correspond to the first maximum of the single-scattering EXAFS oscillation. For decreasing distances the position of the first maximum moves to higher k-values and, thus, higher energies. Simple quantitative considerations lead to Eq. 8 ([21] p 242).

Qualitatively, the bond-length dependence is also easily understood in terms of MOs. Shorter bond lengths correspond to stronger bonding and thus to more negative energies of the bonding MOs and, concomitantly, to an increase in the energy of the anti-bonding MOs. Therefore, as discussed above, the peak resonance and the edge positions are shifted to higher energies. Furthermore, the contribution of the p-orbitals of the X-ray absorbing metal to the bonding MOs may increase and their contribution to the anti-bonding MOs may decrease. The decreased contribution to the anti-bonding MOs will, in tendency, cause an additional contribution to the up-shift of the X-ray edge.

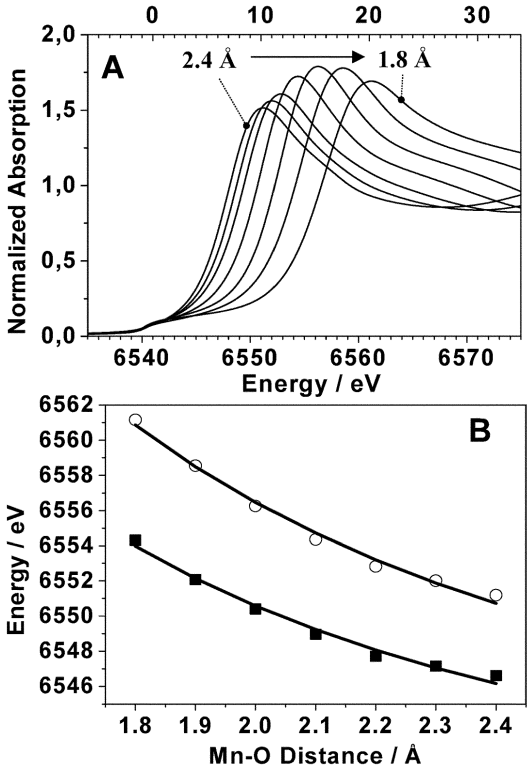

Fig. 15A, B Dependence of calculated XANES spectra on the Mn–O bond length. **A** XANES spectra for a hypothetical, perfectly octahedrally coordinated $Mn(H_2O)_6$ complex calculated for various bond lengths ranging from 2.4 Å to 1.8 Å (from *right to left*, increase in the bond length). **B** Dependence of edge-peak position (*circles*) and edge energy determined by the integral method (*squares*) on the Mn–O bond length. *Solid lines* have been calculated using Eq. 8 and values of A=6537.7 eV, B=75.1 eV/A^2, for the edge-peak position, and of A=6536.1 eV, B=57.9 eV/A^2, for the edge energies

We feel that, at least for Mn coordinated exclusively by O,N ligands, the bond-length dependence of the X-ray absorption spectrum is the major reason for the oxidation-state dependence of the X-ray edge spectra. For oxygen or nitrogen ligands of six-coordinated manganese, typically the bond lengths decrease with increasing oxidation state by 0.1–0.2 Å per one-electron oxidation. The bond-length dependence of the XANES thus translates into an oxidation-state dependence of the X-ray edge position.

Are there further influences of the metal-oxidation state on the XANES spectra? Even though the one-electron oxidation of a metal ion is not coupled to a corresponding increase in positive charge (see, e.g., [86]), a minor increase may occur. Assuming that an increase in the oxidation state results in an increase in the positive charge carried by the X-ray absorbing atom, we can anticipate a lowering of the energy level of the *1 s* core electron. The lower *1 s*-energy should cause a comparable shift of all pre-edge and edge resonances to higher energies. However, at least in the case of manganese, the observed shift in the pre-edge position is significantly smaller than the shift in the edge position; mostly the pre-edge shift is below the detection limit (see Figs 7B and 8). Seemingly, this electrostatic hypothesis can not explain the experimentally observed edge-shifts (or only a minor fraction of it).

Upon oxidation of the metal, the number of vacant non- or anti-bonding MOs of *d*-orbital characteristic increases. Thus, an increased number of transitions to unoccupied *d*-orbitals and a corresponding increase in the pre-edge magnitude can be anticipated. However, a clear correlation between the pre-edge magnitude and the formal oxidation state is not observed. In *K*-edge spectra, the pre-edge magnitude is mostly determined by the transition probability of the formally dipole-forbidden transitions. Thus, even subtle changes in the extent of *p-d* mixing may easily override the influence of an increased number of transitions. Nonetheless, in the future, elaborate quantitative analyses of the fine-structure of the pre-edge feature based on multiplet or MO calculations could result in insights in the electronic structure in general and the oxidation state in particular. We also note that, in comparison to *K*-edge spectra, *L*-edge spectra should reflect the number of vacant *d*-orbital sites more directly, and might even allow for "*d*-hole counting" [12].

By combining the oxidation-state dependence and the calculated bond-length dependence, we obtain edge-shifts which are by about 30% smaller than the experimentally observed edge-shifts. In [87] also, the calculated edge-shifts are significantly smaller than the experimentally determined ones. We have investigated the dependence of the calculated spectra on pure changes in the oxidation state of the complex. Since the FEFF code used for the MS calculations delivers problematic results if the atom cluster considered in the self-consistent field calculation carries a significant net charge, we mimicked the oxidation state by removing an appropriate number of H atoms from the water ligands [88, 89]. The resulting edge-shifts are minimal (clearly less than 0.5 eV per oxidation state), whereas the corresponding MO calculations suggest a more pronounced up-shift in the energies of anti-bonding orbitals (not shown). We consider it to be possible that a (putative) "direct electronic influence" of the oxidation state is underestimated when using the present FEFF code (for possible inadequacies of the presently available MS codes for XANES calculations see [26]).

Linear dichroism in the XANES spectra

To demonstrate the potential of XANES analyses, we will present first attempts to understand the experimental results on the linear dichroism in the XANES spectra of partially uni-directionally oriented samples (see EXAFS section).

In Fig. 16, the spectra collected on PSII membrane particles for angles between the X-ray electric field vector and the sample normal of 15°, 35°, 55°, and 75° are shown. We observe that, in comparison to the 15° spectrum, the edge position is shifted to higher energies in the 75° spectrum by about 0.7 eV. The magnitude of the pre-edge peak is maximal at 75° and minimal at 15°.

In a first attempt to qualitatively model the dichroism in the XANES data, we used a highly simplified structural

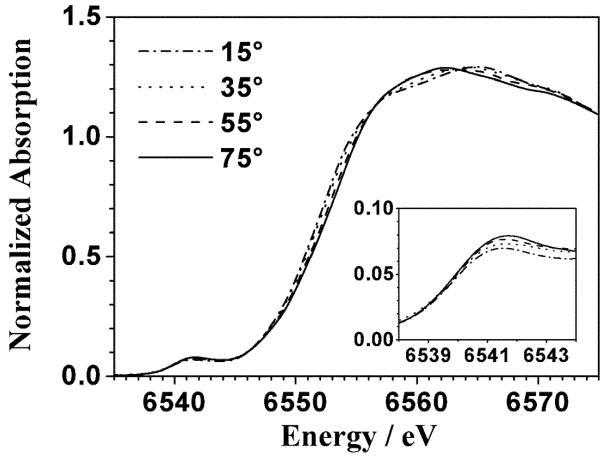

Fig. 16 XANES spectra of the Mn complex of PSII measured at excitation angles (θ_E) of 15°, 35°, 55°, and 75° on partially oriented PSII membrane particles. The *inset* shows the pre-edge region on an expanded energy scale

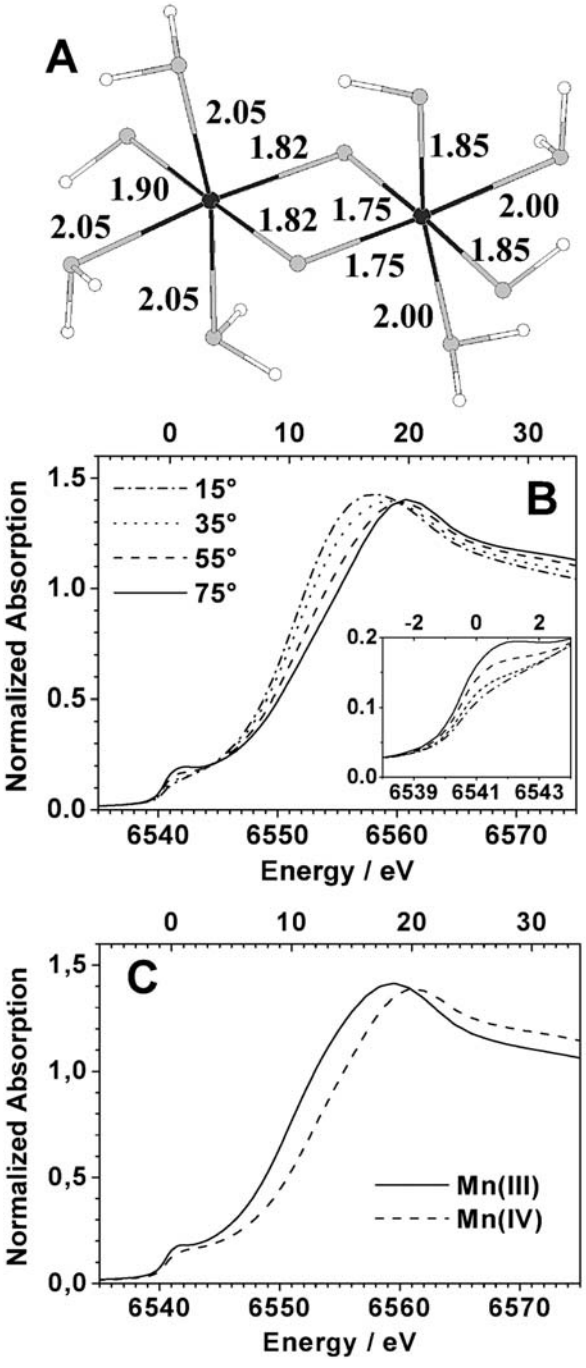

Fig. 17 **A** Structure of a hypothetical di-μ-oxo-bridged manganese complex. The numbers indicate the distances between Mn and its ligands in Å units. **B** Calculated XANES spectra for 4 angles between the electric field vector of the X-ray beam and the Mn–Mn vector. The *inset* shows the pre-edge region on an expanded scale. **C** Calculated XANES spectra for the individual Mn(III) ion and Mn(IV) ion of (**A**) for an excitation angle of 55°. The edge-position of the Mn(III) and Mn(IV)–XANES differ by ~2.8 eV (half-height energies)

model derived from the EXAFS results. In its S_1-state, the PSII manganese complex seems to consist of two di-μ-oxo-bridged Mn_2 units (see Table 1, Fig. 6). The LD–EXAFS analysis shows that in both units the angle between the membrane normal and the Mn–Mn vector is around 70° (Table 1). The dichroism in the first-sphere EXAFS oscillations could indicate that the $Mn_2(\mu\text{–}O)_2$ plane is parallel to the membrane plane rather than perpendicular ([36], Fig. 5, Table 1). The XANES analysis suggests that the Mn complex in its S_1-state is a $Mn_2(III)Mn_4(IV)$ complex (Figs. 7B and 9). To judge whether the FMS calculation can capture the main trends observed in the experimental spectra, we used a model where the two $Mn_2(\mu\text{–}O)_2$ units of the $Mn(III)_2Mn_2(IV)$ complex are modeled by a single Mn(III)–$(\mu\text{–}O)_2$–Mn(IV) unit with the Mn–μO plane being exactly in parallel to the membrane plane, as shown in Fig. 17A. The bond lengths of the six-coordinated Mn ions were chosen to resemble bond lengths of related synthetic compounds. The Mn–O bond lengths of Mn(IV) were significantly shorter than the corresponding Mn(III) bond lengths, and all Mn–μO distances were significantly shorter than the Mn–O distances of the terminal ligands (see Fig. 17A). The number of OH ligands was adjusted such that the overall charge of the complex is zero; the individual atom charges (not shown) are determined in the course of the self-consistent potential calculation by the FEFF8 code. XANES spectra were calculated for various orientations of the X-ray electric field vector. For the XANES spectra (Fig. 17B), the angle between electric field vector and the membrane normal was varied in the plane defined by the membrane-normal direction (perpendicular to the Mn–μO plane) and the vector connecting the two Mn ions; orientation averaging was not employed.

Comparison of Fig. 17B and Fig. 16 shows that the angle-dependent changes in the edge position and in the pre-edge magnitude are qualitatively reproduced by the calculations. The extent of the linear dichroism (meaning the excitation angle-dependence of the XANES spectra), however, is clearly greater in the calculated than in the experimental spectra. This is not surprising for the following reasons:

1. The samples used in the actual XAS experiment have not been perfectly oriented. The order parameter [60] was close to 0.5 indicating that the magnitude of the dichroism in a perfectly oriented sample would be greater by a factor of two.
2. In the PSII manganese complex the $Mn_2(\mu O)_2$ plane certainly is not perfectly parallel to the membrane plane.
3. The samples had been only uni-directionally oriented such that appropriate angle averaging of calculated XANES spectra is required for any quantitative comparison with experimental results. (We are currently working on a method to employ available MS–XANES codes for fully quantitative simulation of the XANES dichroism of partially uni-directionally oriented samples; Liebisch & Dau, manuscript in preparation).

The main features of the observed and calculated XANES dichroism are explainable by considering the orientation and properties of the relatively short Mn–μO bonds. To explain the angle-dependence of the edge qualitatively, simple single-scattering considerations are sufficient. The short bond lengths of the Mn–μO bonds are preferentially probed when the excitation angle, Θ_E, approaches 90°. On the other hand, for Θ_E-values close to 0° the amplitude of the single-scattering XAFS mostly is determined by the longer bonds of the terminal ligands. Due to the bond-length dependence of the edge position (Fig. 15, Eq. 8), we can predict an increase in the edge position with increasing Θ_E. (Using the MO picture, we may conclude that the short Mn–μO bonds correspond to higher energies of the respective antibonding *p*-type MOs which are oriented along the Mn–μO or Mn–Mn axes. Transitions to these high-energy MOs are not excited by X-rays with the electric field vector being perpendicular to the $Mn_2(\mu O)_2$ plane.)

On the basis of multiple considerations, it has been concluded that the pre-edge magnitude of the PSII manganese complex is significantly increased in comparison to the pre-edge magnitude found for mono-nuclear manganese complexes due to the presence of the di-μ-oxo-bridges [90]. We feel that the angle-dependence of the pre-edge magnitude can also be attributed to a coordination geometry involving short Mn–μO bonds and distinctly longer bonds between the Mn and its terminal ligands. This geometry partially breaks the inversion symmetry at the X-ray absorbing manganese and facilitates increased *p*-*d*-mixing. Consequently, the pre-edge feature gains significant intensity. The *p*-*d*-mixing will involve mostly *p*-orbitals of the $Mn_2(\mu\text{–}O)_2$ plane. These *p*-orbitals will affect the X-ray absorption strongly only for Θ_E-values close to 90°, resulting in an increased pre-edge magnitude for Θ_E-values approaching 90°.

In general, the FEFF code used seems to overestimate the magnitude of the pre-edge feature of six-coordinated manganese by a factor of about two. This is not particularly surprising because the MS calculations can be anticipated to be of lower precision for low-lying bound states. Comparison of the simulated Mn–hexaquo spectra and the $Mn_2(\mu\text{–}O)_2$ spectra shows that, in both cases, the pre-edge magnitude is clearly greater than in the corresponding experimental spectra. However, the MS calculations correctly predict a significantly higher pre-edge feature in the di-μ-oxo-bridged manganese complex.

We consider this preliminary work on the simulations of the linear dichroism in the XANES spectra to be promising. In the future, an iterative cycle of EXAFS analysis, model building, LD–XANES simulations, and comparison between data and calculations may turn out to be useful for derivation of detailed structural models of the metal complex and its ligand environment (work in progress).

Conclusions

XAS spectroscopy can provide a wealth of information on the nuclear geometry and electronic structure of protein-bound metal complexes, which is frequently not accessible by other means. However, not all aspects of interest can be addressed by the BioXAS method and the information carried by the spectra is not always easily extracted, as summarized in the following sections.

EXAFS distances

The EXAFS part of the X-ray absorption spectrum provides the primary tool for development of atomic-resolution structural models. Its major strength is that bond lengths can be determined at an accuracy that is typically better than 0.02 Å. This is superior to accuracies normally available from protein crystallography by approximately one order of magnitude. A limitation of the EXAFS method is that it is a short-range method. First-sphere ligands are nearly always seen, more distant atoms may be resolvable, and atoms more than 5 Å away cannot usually be detected. Heavy backscatterers (e.g., transition ions) at distances below 4 Å are mostly visible, an important benefit in investigations on multinuclear metal complexes. In the case of ligand shells with a broad distribution of distances, EXAFS also has only limited bond length resolution and often only the average bond length can be determined at high accuracy. If the first coordination sphere consists of two distinct distance-groups of atoms with the two mean distances differing by at least 0.1 Å, then the two distances can be resolved individually, a situation frequently encountered in metal centers with O,N ligands on the one hand, and sulfur ligands on the other hand (see, e.g., [91]). If the radial distribution function of the metal ligands is broad, but without well-resolved maxima, then the average distance and an approximate description of the distance distribution function (or radial distribution function) can be extracted from the EXAFS data.

EXAFS coordination numbers

The accurate determination of coordination numbers by EXAFS analysis is not readily achieved. Due to the typical inaccuracy of 20%, the distinction between (e. g.) coordination by five or six first-sphere ligands cannot be made solely by analysis of a single EXAFS data set. Furthermore, in the case of extremely broad distance distributions within a single coordination sphere, the error in the coordination number may clearly exceed 20%, if inappropriate simulation approaches are used. An improved determination of coordination numbers can result from the comparative or joint analysis of extended sets of EXAFS data obtained by different *k*-weighting of data, use of active-site mutants, pH or substrate titration, time-resolved investigations, temperature-dependent XAS measurements, angle-dependent measurements on oriented samples (polarized or LD–EXAFS), etc. Furthermore, XANES analysis may also contribute to solving of the coordination number problem.

Atomic resolution models

The development of atomic resolution models of the metal site mostly requires input from various sources (sequence information or mutant studies, identification of ligating residues, complementary results by other spectroscopic techniques or protein crystallography, extensive XAS studies involving, e.g., metal depletion and replacement by other elements). Only if (partially) oriented samples or single crystals of an appropriate space-group are available, can information on the orientation of the metal complex with respect to the tertiary structure of the protein become accessible by linear dichroism EXAFS studies (polarized or angle-dependent EXAFS).

Structural information in XANES

The *K*-edge XANES spectra carry significant structural information. The use of the edge position as a ruler for the first-sphere bond length is not of high interest due to its inferior accuracy (about ±0.1 Å versus ±0.02 Å in EXAFS). However, XANES analysis seems to be superior to EXAFS with respect to the determination of first-sphere coordination numbers and, in particular, coordination geometries. By comparison with model compound spectra and/or calculations, the structural information of the XANES may become accessible. Recently the fit of XANES spectra by variation of structural parameters has also been approached [92, 93].

XANES and electronic structure

In the MO picture, the edge region of *K*-edge spectra reflects transitions to non- and anti-bonding MOs with (some) *p*-orbital character. It should be noted that the relevant MOs are closely related, but not identical to the ground-state MOs of the metal complex. For quantitative XANES analysis, less approximate considerations may be required, which account for the influence of electronic relaxation, core-hole screening, and other multi-electron effects. Due to the interdependence of nuclear geometry and electronic structure, a quantitative description can be obtained by using advanced multiple scattering (MS) theories. Current MS theory may not cover all relevant aspects of the electronic structure and its relation to the XANES spectra (see also [26]); further improvements are desirable.

Oxidation-state dependence of XANES

Empirically, a correlation between *K*-edge position and oxidation state is frequently found. However, the *K*-edge edge spectra are not directly related to the oxidation state of the transition metal. Neither the metal charge nor the occupancy of non- and anti-bonding *d*-orbitals affect the edge position directly. A major cause of the *K*-edge shift seems to be an increase in the bonding strength of the first-sphere ligands causing an up-shift in the energy of the anti-bonding orbitals and a decrease in the bond length. We note that for protein-bound manganese the situation may be less intricate than in other systems: metal-localized valencies seem to prevail so that the integrated spin density of the individual high-spin Mn ions (and thus the number of singly occupied non- and anti-bonding *d*-type MOs) corresponds directly to the respective oxidation state. However, especially in the presence of sulfur ligands, spin density may also reside on first-sphere ligands of the transition metal so that (1) the true metal oxidation state is no longer well-characterized by a single integer number and (2) an increase in the (overall) oxidation state of the complex does not necessarily result in shortening of the metal–ligand bonds. Other X-ray spectroscopy techniques (for review see [94]), such as *L*-edge spectroscopy, inelastic X-ray scattering and, perhaps, analysis of the K_β fluorescence (including site-selective XAS) may provide more direct access to the metal oxidation state. The general value of these techniques for investigations on protein-bound metal centers still needs to be shown.

Methods of XANES analysis

The most used approach to relate XANES spectra and formal oxidation state is purely empirical. It has been successfully used, but unambiguous results are not necessarily obtained. Only small edge-shifts can be anticipated, especially in the case of multinuclear complexes, and the choice of the method used to determine edge-positions gains critical importance. In the future, more advanced XANES analysis methods involving MS and/or MO calculations could allow for unambiguous oxidation state assignments, and more of the information carried by the XANES on the electronic structure and the nuclear geometry may become accessible.

Acknowledgement We thank Drs Hilmar Schiller, Lucia Iuzzolino, Jens Dittmer, Wolfgang Dörner, and Pavel Pospisil as well as Markus Grabolle and Claudia Müller for collection and analysis of XAS data on the PSII manganese complex discussed in this study. The respective BioXAS experiments have been carried out in cooperation with Drs Hans Nolting and Wolfram Meyer-Klaucke at the XAS beamline of the EMBL outstation Hamburg (HASYLAB/DESY, Hamburg). We thank them and the staff of the EMBL outstation for support. Financial support by the German Bundesministerium für Forschung und Technologie (BMBF, program: Erforschung kondensierter Materie, project 05KS1KEA/6) and the Deutsche Forschungsgemeinschaft (DFG, TP C6 and TP C8 in the SFB 498, Berlin) is gratefully acknowledged.

References

1. Lippard SJ, Berg JM (1994) Principles of bioinorganic chemistry. University Science Books, Sausalito
2. Cowan JA (1996) Inorganic biochemistry: an introduction. Wiley, New York
3. Hill HAO, Sadler PJ, Thomson AJ (1999) Metal sites in proteins and models. Springer, Berlin Heidelberg New York
4. Yachandra VK (1995) Meth Enzymol 246:638–678
5. George GN, Hedman B, Hodgson KO (1998) Nature Struc Biol – Synchrotron Supplement:645–647
6. Scott RA (2000) In: Que L (ed) Physical methods in bioinorganic chemistry – spectroscopy and magnetism. University Science Books, Sausalito, pp 465–504
7. Dau H, Haumann M (2003) J Synchrotron Rad 10:76–85
8. Special issue on BioXAS (2003) J Synchrotron Rad 10(1)
9. Dau H, Dittmer J, Epple M, Hanss J, Kiss E, Rehder D, Schultze C, Vilter H (1999) FEBS Lett 457:237–240
10. Peariso K, Zhou ZS, Smith AE, Matthews RG, Penner-Hahn JE (2001) Biochemistry 40:987–993
11. Wang H, Peng G, Miller LM, Scheuring EM, George SJ, Chance MR, Cramer SP (1997) J Am Chem Soc 119:4921–4928
12. Wang H, Ge P, Riordan CG, Brooker S, Woomer CG, Collins T, Melendres CA, Graudejus O, Bartlett N, Cramer SP (1998) J Phys Chem B 102:8343–8346
13. Wang H, Patil DS, Gu W, Jacquamet L, Friedrich S, Funk T, Cramer SP (2001) J Electron Spectrosc Relat Phenom 114–116:855–863
14. Cramer SP, DeGroot FMF, Ma Y, Chen CT, Sette F, Kipke CA, Eichhorn DM, Chan MK, Armstrong WH, Libby E, Christou G, Brooker S, McKee V, Mullins C, Fuggleg JC (1991) J Am Chem Soc 113:7937–7940
15. Ralston CY, Wang HX, Ragsdale SW, Kumar M, Spangler NJ, Ludden PW, Gu W, Jones RM, Patil DS, Cramer SP (2000) J Am Chem Soc 122:10553–10560
16. DeBeer GS, Metz M, Szilagyi RK, Wang H, Cramer SP, Lu Y, Tolman WB, Hedman B, Hodgson KO, Solomon EI (2001) J Am Chem Soc 123:5757–5767
17. Meinke C, Sole AV, Pospisil P, Dau H (2000) Biochemistry 39:7033–7040
18. Haumann M, Grabolle M, Neisius T, Dau H (2002) FEBS Lett 512:116–120
19. Ascone I, Meyer-Klaucke W, Murphy L (2003) J Synchrotron Rad 10:16–22
20. Haumann M, Pospisil P, Grabolle M, Müller C, Liebisch P, Sole AV, Neisius T, Dittmer J, Iuzzolino L, Dau H (2003) J Synchrotron Rad 10:76–85
21. Stöhr J (1992) NEXAFS spectroscopy. Springer, Berlin Heidelberg New York
22. Rehr JJ, Albers RC (2000) Rev Mod Phys 72:621–654
23. Teo BK (1986) EXAFS: basic principles and data analysis. Springer, Berlin Heidelberg New York
24. Koningsberger DC, Mojet BL, vanDorssen GE, Ramaker DE (2000) Topics in catalysis 10:143–155
25. Binsted N, Hasnain SS (1996) J Synchrotron Rad 3:185–196
26. Natoli CR, Benfatto, M, Della Longa S, Hatada K (2003) J Synchrotron Rad 10:26–42
27. Ankudinov AL, Ravel B, Rehr JJ, Conradson SD (1998) Phys Rev B 12:7565–7576
28. Kirby JA, Robertson AS, Smith JP, Thompson AC, Cooper SR, Klein MP (1981a) J Am Chem Soc 103:5529–5537
29. Kirby JA, Goodin DB, Wydrzynski T, Robertson AS, Klein MP (1981b) J Am Chem Soc 103:5537–5542
30. MacLachlan DJ, Hallahan BJ, Ruffle SV, Nugent JH, Evans MC, Strange RW, Hasnain SS (1992) Biochem J 285:569–576
31. Ono T, Nogushi T, Inoue Y, Kusunoki M, Matsushita T, Oyanagi H (1992) Science 258:1335–1337
32. Penner-Hahn JE (1999) In: Hill HAO, Sadler PJ, Thomson AJ (eds) Metal sites in proteins and models: redox centres. Springer, Berlin, Heidelberg New York, pp 1–36
33. Robblee JH, Cinco RM, Yachandra VK (2001) Biochim Biophys Acta 1503:7–23
34. Dau H, Iuzzolino L, Dittmer J (2001) Biochim Biophys Acta 1503:24–39
35. Iuzzolino L, Dittmer J, Doerner W, Meyer-Klaucke W, Dau H (1998) Biochemistry 37:17112–17119
36. Schiller H, Dittmer J, Iuzzolino L, Doerner W, Meyer-Klaucke W, Sole VA, Nordstroem T, Dau H (1998) Biochemistry 37: 7340–7350
37. Schiller H, Dau H (2000) J Photochem Photobiol B 55:138–144
38. Pospisil P, Haumann M, Dittmer J, Sole AV, Dau H (2003) Biophys J 84:1370–1386
39. Dittmer J, Iuzzolino L, Dörner W, Nolting, H-F, Meyer-Klaucke W, Dau H (1998) In: Garab G (ed) Photosynthesis: mechanism and effects, vol II. Kluwer, Dordrecht, pp 1339–1342
40. Zerner MC, Loew GH, Kirchner RF, Mueller-Westerhoff UT (1980) J Am Chem Soc 102:589–599
41. Stavrev KK, Zerner MC (1995) J Chem Phys 102:34–38
42. Stavrev KK, Zerner MC, Meyer TJ (1995) J Am Chem Soc 117:8684–8685
43. Sayers DE, Stern, EA, Lytle FW (1971) Phys Rev Lett 27: 1204–1207
44. Gurman SJ, Binsted N, Ross I (1983) J Phys C 17:143–151
45. Gurman SJ (1988) J Phys C 21:3699–3717
46. Mustre de Leon J, Yacoby Y, Stern EA, Rehr JJ (1990) Phys Rev B 42:10843–10851
47. Mustre de Leon J, Rehr JJ, Zabinsky SI, Albers RC (1991) Phys Rev B 44:4146–4156
48. Rehr JJ, Ankudinov AL (2001) J Synchrotron Rad 8:61–65
49. Ashley CA, Doniach S (1975) Phys Rev B 11:1279–1288
50. DeRose VJ, Latimer MJ, Zimmermann JL, Mukerji I, Yachandra VK, Sauer K, (1995) Chem Phys 194:443–459
51. Robblee JH, Messinger J, Cinco RM, McFarlane KL, Fernandez C, Pizarro SA, Sauer K, Yachandra VK (2002) J Am Chem Soc 124:7459–7471
52. Dörner W, Dittmer J, Iuzzolino L, Dau H (1998) In: Garab G (ed) Photosynthesis: mechanism and effects, vol II. Kluwer, Dordrecht, pp 1343–1346
53. Latimer MJ, DeRose VJ, Mukerji I, Yachandra VK, Sauer K, Klein MP (1995) Biochemistry 34:10898–10909
54. Cinco RM, Robblee JH, Rompel A, Fernandez C, Yachandra VK, Sauer K, Klein MP (1998) J Phys Chem B 102:8248–8256
55. Cinco RM, McFarlane Holman KL, Robblee JH, Yano J, Pizarro SA, Bellacchio E, Sauer K, Yachandra VK (2002) Biochemistry 41:12928–12933
56. Haumann M, Grabolle M, Werthammer M, Iuzzolino L, Dittmer J, Meyer-Klaucke W, Neisius T, Dau H (2001) In: PS2001 Proceedings. CSIRO, Collingwood, Australia, contribution S10–013, pp 1–5
57. Koningsberger DC (1994) In: Baruchel J, Hodeau JL, Lehmann MS, Regnard JR, Schlenker C (eds) Neutron and synchrotron radiation for condensed matter studies, vol II. Springer, Berlin Heidelberg New York, p 213
58. Mukerji I, Andrews JC, DeRose VJ, Latimer MJ, Yachandra VK, Sauer K, Klein MP (1994) Biochemistry 33:9712–9721

59. Dau H, Andrews JC, Roelofs TA, Latimer MJ, Liang W, Yachandra VK, Sauer K, Klein MP (1995) Biochemistry 34: 5274–5287
60. Dittmer J, Dau H (1998) J Phys Chem B 102:8196–8200
61. Benfatto M, Natoli CR, Brouder C, Pettifer RF, Ruiz López MF (1989) Phys Rev B 39:1936–1939
62. Binsted N, Strange RW, Hasnain SS (1992) Biochemistry 31: 12117–12125
63. Pettifer RF, Brouder C, Benfatto M, Natoli CR, Hermes C, Ruiz López MF (1990) Phys Rev B 42:37–42
64. Zouni A, Witt H-T, Kern J, Fromme P, Krauß N, Saenger W, Orth P (2001) Nature 409:739–743
65. Yachandra VK (2002) Philos Trans R Soc Lond B Biol Sci 357:1347–1357
66. Carrell G, Tyryshkin M, Dismukes C (2002) J Biol Inorg Chem 7:2–22
67. Sauer K, Yachandra VK, Britt RD, Klein M (1992) In: Pecoraro VL (ed) Manganese redox enzymes. VCH, New York, pp 85–103
68. Bossek U, Hummel H, Weyhermüller T, Wieghardt K, Russel S, van der Wolf L, Kolb W (1996) Angew Chem 108:1653–1656
69. Stemmler TL, Sossong TM Jr, Goldstein JI, Ash DE, Elgren TE, Kurtz DM Jr, Penner-Hahn JE (1997) Biochemistry 36: 9847–9858
70. Roelofs TA, Liang W, Latimer MJ, Cinco RM, Rompel A, Andrews JC, Sauer K, Yachandra VK, Klein M (1996) Proc Natl Acad Sci USA 93:3335–3340
71. Messinger J, Robblee JH, Bergmann U, Fernandez C, Glatzel P, Visser H, Cinco RM, McFarlane KL, Bellacchio E, Pizarro SA, Cramer SP, Sauer K, Klein MP, Yachandra VK (2001) J Am Chem Soc 123:7804–7820
72. Visser H, Anxolabehere-Mallart E, Bergmann U, Glatzel P, Robblee JH, Cramer SP, Girerd JJ, Sauer K, Klein MP, Yachandra VK (2001) J Am Chem Soc 123:7031–7039
73. Dismukes GC, Siderer Y (1981) Proc Natl Acad Sci USA 78: 274–278
74. Miller A-F, Brudvig GW (1991) Biochim Biophys Acta 1056: 1–18
75. Messinger J, Nugent JHA, Evans MCW (1997) Biochemistry 36:11055–11060
76. Åhrling KA, Peterson S, Styring S (1998) Biochemistry 37: 8115–8120
77. Boussac A, Kuhl H, Ghibaudi E, Rögner M, Rutherford AW (1999) Biochemistry 38:11942–11948
78. Dittmer J (1999) PhD thesis, Christian-Albrechts-Universität Kiel, Germany
79. Winstead CL, Langhoff PW (1988) Chem Phys Lett 151:417–424
80. Gil TJ, Winstead CL, Langhoff PW (1989) Comp Phys Comm 53:123–131
81. Gil TJ, Winstead CL, Sheehy JA, Farren RE, Langhoff PW (1990) Physica Scripta T31(Proc Int Conf Vac Ultraviolet Rad Phys, 9th, 1989):179–188
82. Kasrai M, Fleet ME, Bancroft GM, Tan KH, Chen JM (1991) Phys Rev B 43:1763–1772
83. Riggs-Gelasco PJ, Penner-Hahn JE (1995) Adv Chem Ser 246: 219–248
84. Lytle FW, Greegor RB and Panson A J (1988) Phys Rev B 37: 1550–1562
85. Sheehy JA, Gil TJ, Winstead CL, Farren RE, Langhoff PW (1989) J Chem Phys 91:1796–1812
86. Blomberg MRA, Siegbahn PEM, Styring S, Babcock GT, Akermark B, Korall P (1997) J Am Chem Soc 119:8285–8292
87. Mijovilovich A, Meyer-Klaucke W (2003) J Synchrotron Rad 10:64–68
88. Frenkel AI, Ankudinov AL, Korshin GV (2000) Environ Sci Technol 34:2138–2142
89. Merkling PJ, Munoz-Paez A, Pappalardo RR, Sanchez ME (2001) Phys Rev B 64(92201):1–4
90. Kusunoki M, Ono T, Matsushita T, Oyanagi H Inoue Y (1990) J Biochem 108:560–567
91. Krüer M, Haumann M, Meyer-Klaucke W, Thauer KR, Dau H (2002) Eur J Biochem 269:2117–2123
92. Benafetto M, Della Longa S (2001) J Synchrotron Rad 81087–1094
93. Della Longa S, Arcovito A, Girasole M, Hazemann JL, Benfatto M (2001) Phys Rev Lett 87:155501
94. De Groot F (2001) Chem Rev 101:1779–1808